2006

Exploring the hot-carrier effect on the wireless transceivers

Sameer R. Herlekar
Louisiana State University and Agricultural and Mechanical College, sherle1@lsu.edu

EXPLORING THE HOT-CARRIER EFFECT ON THE WIRELESS TRANSCEIVERS

A Dissertation

Submitted to the Graduate Faculty of the
Louisiana State University and
Agricultural and Mechanical College
in partial fulfillment of the
requirements for the degree of
Doctor of Philosophy

in

The Department of Electrical and Computer Engineering

by
Sameer Raja Herlekar
B. E., Birla Institute of Technology and Science, 1999
M. Sc., Birla Institute of Technology and Science, 1999
M. S., Louisiana State University, 2001
August 2006

Dedicated to my family
Prof. R. K. Herlekar, Father
Sudha R. Herlekar, Mother
Vikram R. Herlekar, Brother

Acknowledgements

I would like to sincerely acknowledge the unwavering support and guidance provided by my major professor, Dr. Hsiao-Chun Wu during the course of this study. His guidance not only helped me in formulating the research problem and in maintaining my focus throughout my doctoral research, but will also go a long way in helping me in my professional career. I am deeply grateful to Dr. Wu for his support, encouragement and guidance throughout my graduate studies at LSU.

I am very thankful to Dr. Ashok Srivastava for his invaluable assistance with the phase noise modeling, which helped in my research work being accepted for premier IEEE and SPIE conferences. His precious support and guidance throughout my doctoral studies at LSU is gratefully acknowledged.

My heartfelt thanks and sincere appreciation are due to Dr. Subhash Kak for his invaluable suggestions and advices for me when I would report my research progress to him, for the many professional discussions I had with him from which I learnt so much, and for his constant encouragement and support throughout my graduate study.

I am also very thankful to Dr. Jurgen Hurrelbrink, Dr. Peter Wolenski and Dr. Jianhua Chen for their unflinching support and encouragement, and for their precious suggestions for me when I would report my research findings to them.

I would like to thank Mr. Chi Zhang for his help with the phase noise modeling and with the theory of MOSFET device electronics.

I am very grateful to Dr. Stefan Kaiser, Head of Wireless Solution Laboratory at DoCoMo Euro-Labs, Munich, Germany, for his kind help and invaluable suggestions for the research results found in Chapter 2.

My sincere thanks are due to my good friend Dr. Nikhil Gupta, Polytechnic University, Brooklyn, N.Y. for his constant support and encouragement throughout my doctoral studies.

I also would like to acknowledge the support and encouragement from my research group mates. It has been a pleasure working with all of them over the last several months.

I express my grateful appreciation to my good friend, Mr. Phalguna Kumar Rachinayani, for his encouragement and support during my doctoral studies.

Last, but by no means the least, I wish to acknowledge the unconditional love and support provided by my family throughout my life.

Table of Contents

List of Acronyms

ADC:	Analog-to-digital converter
ADSL:	Asymmetrical digital subscriber line
AWGN:	Additive white Gaussian noise
BER:	Bit error rate
CFO:	Carrier-frequency offset
CMOS:	Complementary metal-oxide semiconductor
CP:	Cyclic prefix
CPE:	Common phase error
DAB:	Digital audio broadcasting
DAC:	Digital-to-analog converter
DFT:	Discrete Fourier transform
DVB-T:	Digital video broadcasting – terrestrial
EVM:	Error vector magnitude
HC:	Hot-carrier
ICI:	Inter-carrier interference
IDFT:	Inverse discrete Fourier transform
ISI:	Inter-symbol interference
kHz:	Kilohertz
LF:	Loop filter
LPF:	Low-pass filter
LSB:	Least significant bit

MHz:	Megahertz
MOSFET:	Metal-oxide semiconductor field-effect transistor
MSB:	Most significant bit
OFDM:	Orthogonal frequency division multiplexing
OOB:	Out-of-band
PAPR:	Peak-to-average power ratio
PD:	Phase detector
PDF:	Probability density function
PLL:	Phase-locked loop
PSD:	Power spectral density
PSK:	Phase-shift-keying
QAM:	Quadrature amplitude modulation
QoS:	Quality-of-service
QPSK:	Quadrature phase-shift-keying
RF:	Radio frequency
SC:	Self-cancellation
SINR:	Signal-to-interference plus noise ratio
SNR:	Signal-to-noise-ratio
TDMA:	Time-division multiple-access
VCO:	Voltage-controlled oscillator
WLAN:	Wireless local area network
WMAN:	Wireless metropolitan area network

Abstract

Phase noise can be regarded as the most severe cause of performance degradation in the wireless communication systems. The hot-carriers (HCs), found in the CMOS synchronization circuits, are the high-energy charge carriers that degrade the MOSFET devices' performance by increasing the threshold voltage required to operate the MOSFETs. The HC effect manifests itself as the phase noise whose level increases with the continued MOSFET operation and such increases result in the performance degradation of the voltage-controlled oscillator (VCO) built on the MOSFETs. The HC effect is particularly evident in the short-channel MOSFET devices. In this dissertation, we analyze the wireless transceiver performances in the presence of the synchronization errors induced by the HC effect, for both single-carrier and multi-carrier communication systems. We derive the relationship between the corresponding system performances and the HC effect in terms of a crucial parameter, the MOSFET threshold voltage. We employ a new phase noise model for the wireless systems influenced by the HC effect, which is based on a new precise phase noise mask function. In addition, we analyze the impact of the phase noise arising from the HC effect on the single-carrier wireless systems in terms of the BER and the signal-to-interference-plus-noise ratio (SINR). We derive the exact BER expression and show the SINR degradation for the QPSK systems that suffer from the phase noise. We apply Monte Carlo simulations to verify our analysis. To study the HC effect thoroughly, we simplify the BER expression as a new asymptotical analysis as the signal-to-noise ratio approaches to infinity and obtain the lower bound of the achievable BER for the single-carrier wireless systems. For multi-

carrier systems, we focus our discussions on the orthogonal frequency division multiplexing (OFDM) systems. According to our simulations, we show that the bit-error-rate (BER) evaluation for OFDM using our new phase noise model in the presence of the HCs can be very different up to three orders-of-magnitude from the existing models disregarding the HCs. We have also found that the ICI self-cancellation coding is very effective for combating the phase noise in the OFDM systems.

Chapter 1

Introduction

1.1 Overview

Telecommunication plays a major role in our daily lives. For example, we converse almost daily on the wired or wireless telephone. Electronic mail, or e-mail, is a means by which we exchange text or graphical information with our friends and colleagues. Personal digital assistants (PDAs) have become an indispensable part in the corporate world. Nowadays, wireless services dominate the consumers' market demand. Such devices include (but are not limited to) cellular phones, wireless local area networking (WLAN) adapters, PDAs and stationary/mobile digital television (DTV) receivers.

The recent proliferation of the wireless technology has resulted in a tremendously increasing demand for *compact* complimentary metal-oxide semiconductor (CMOS) devices. These CMOS devices, also known as the *short-channel* CMOS devices, form the electronic building blocks of the crucial synchronization circuits such as the phase-locked loops (PLLs) found in the wireless transceivers. However, these CMOS devices suffer from a phenomenon called the *hot-carrier (HC) effect* which increases the phase noise levels in the CMOS. As studied in Section 1.4, phase noise manifests itself as a spillage of the transmitted signal power from the central (carrier) frequency onto the adjacent frequencies. Consequently, the performance of a CMOS device deteriorates over time. Thus, it can be conjectured that the performance of the parent wireless device built on top of the short-channel CMOS would also degrade over time. In this dissertation, we will analyze the impact of the HC effect on (1) the wireless systems based on the conventional *single-carrier* modulation, and (2) the

wireless systems based on orthogonal frequency division multiplexing (OFDM) or *multi-carrier* modulation.

The results presented in this dissertation can serve as an invaluable guide for the design of the modern wireless communication transceivers which are built on the short-channel CMOS devices. For example, the quality-of-service (QoS) performance of a wireless transceiver built on the compact CMOS devices can be predicted using the analysis and simulation results which we will provide in this dissertation. The QoS performance measures under investigation here are the bit-error-rate (BER) and the signal-to-interference-plus-noise ratio (SINR).

1.2 Phase-Locked Loop (PLL)

The aforementioned synchronization circuits play a crucial role in the wireless transceiver's performance. They perform phase synchronization, frequency synchronization and symbol (timing) synchronization for the receiver with respect to the transmitted signal's phase, frequency and symbol timing, respectively. A typical example is the *phase-locked loop* (PLL). The general PLL diagram is depicted in Figure 1.1. Basically, the PLL consists of three main components, namely the *phase detector* (PD), the *loop filter* (LF), and the *voltage-controlled oscillator* (VCO), as shown in Figure 1.1.

As shown in Figure 1.1, the PD generates the signal $e(t)$ which is a measure of the difference or error, $|\theta| = |\angle x(t) - \angle u(t)|$, between the phase of the incoming signal, $\angle x(t)$, and the phase of the local carrier signal, $\angle u(t)$, generated by the VCO [1, 2]. $e(t)$ is the driven signal to the LF for generating the appropriate voltage $v(t)$ such that it can control the VCO to minimize the aforementioned phase error $|\theta|$. The primary purpose of the VCO

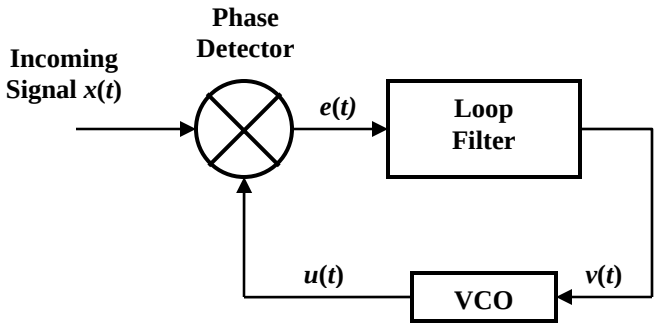

Figure 1.1. The basic PLL structure.

is to generate the local carrier signal $u(t)$ whose phase $\angle u(t)$ closely matches the phase of the incoming signal $\angle x(t)$. The carrier signal $u(t)$ is used for the frequency down-conversion in the demodulator of the wireless communication receiver. Therefore, the PLL is known to *synchronize,* in phase and frequency, the receiver's local carrier signal with the received signal. The error signal $e(t)$ is a *time-varying* voltage waveform, since the phase difference is time-varying in nature. The LF suppresses the high frequency signal and noise components, and also helps determine the PLL dynamic performance [1]. A well-designed PLL reliably tracks the changes in the phase difference between the carriers and its performance is insensitive to the receiver noise [2]. However, it is noted that digital PLLs often possess an operating loop delay which can affect the stability, especially when the loop bandwidth is large during the signal acquisition stage [3]. The performance of wireless systems which are based on the coherent phase modulation such as phase-shift-keying (PSK) is highly dependent on the synchronization performance of the PLL [2]. When the PLL is unable to synchronize the local carrier signal $u(t)$ with the incoming signal $x(t)$ (i.e., a significant phase error $|\theta|$ exists in between), the overall performance of the wireless system is

degraded. As will be studied briefly in Sections 1.3 and in detail in Chapters 2-4, a major cause of the PLL's failure to synchronize the local carrier signal with the received signal is the phase noise generated by the short-channel CMOS devices found in the PLL hardware.

The PLL is normally found in both transmitter and receiver of a communication system. However, for simplicity, we focus on the PLL operation in the receiver only. As a matter of fact, the communication circuitry in the transmitter is often much more sophisticated than that in the receiver, and therefore the PLL operation in the receiver usually is the major concern for the wireless system performance evaluation [4, 5].

1.3 MOSFET Electronics and the Hot-carrier Effect in Modern Wireless Transceivers

The phase error due to the PLL devices, as described Section 1.2, is aggravated when those PLLs are made of short-channel devices for high oscillating frequencies. To study this short-channel effect, we consider here the metal-oxide-semiconductor field-effect transistor (MOSFET), whose cross-sectional view is shown in Figure 1.2. In modern communication receivers, the MOSFET forms an integral part of the PD, the LF and the VCO [6], which belong to the radio-frequency front-end of the receivers.

According to Figure 1.2, in the stand-alone condition of the n-type MOSFET, electrons (also called *charge-carriers*) reside in the *source* (S) and the *drain* (D) regions of the MOSFET. When a voltage is applied between the *gate* (G) and the source (S), an electric field is created between the source and the drain terminals [7].

If this applied voltage exceeds a critical value known as the *threshold voltage* (V_{th}), the oxide-layer field begins to draw electrons from the source into the substrate region below the gate. The layer of electrons thus created between the source and the drain is termed the

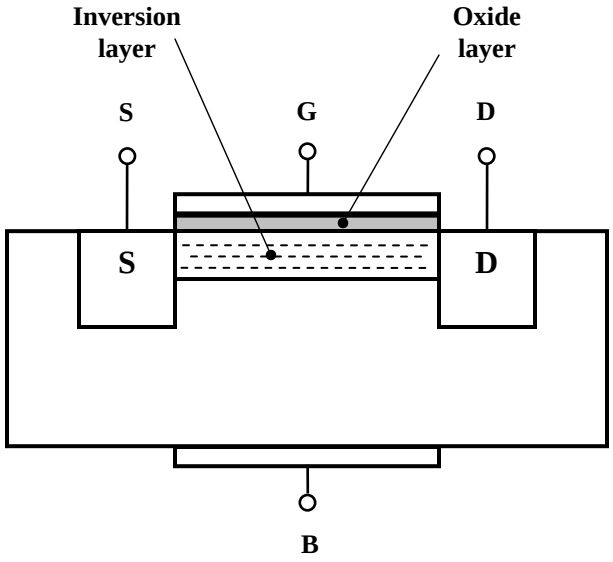

Figure 1.2. Cross-sectional view of an n-type MOSFET.

inversion layer, as illustrated in Figure 1.2 [7]. The electrons acquire sufficient energy to travel across the inversion layer from the source into the drain end of the MOSFET. The MOSFET is then said to be *on*, or under operation. During normal MOSFET operation, the *body* (B) terminal is often connected to the source and is hence at the same potential as S. An n-type MOSFET, when arranged in a complementary fashion with a p-type MOSFET, constitutes the well-known complementary-MOS (CMOS) configuration [7].

With the recent proliferation of wireless technology [8-15], the demand for *compact* CMOS devices has increased tremendously. Such CMOS devices possess a short channel between the drain and the source, of the order of sub-microns [6]. However, these short-channel devices are very sensitive to the *hot carrier effect* in the MOSFET structure. The hot carriers (HCs) are charge-carriers that have been highly energized by the electric fields inside the MOSFET device. They destroy the device structure by creating electron interface traps and oxide-trapped charges, and alter [16] the device parameters such as the *threshold voltage*

increase in n-channel MOSFET devices, and the *tuning range decrease* of the VCO built on the CMOS electronics. The influence of HCs on the radio-frequency circuitry performance has been extensively analyzed in terms of the *minimum noise figure*, *cut-off frequency* and *maximum frequency* in [17].

It has also been shown that the HC effect in the MOSFET can enlarge the phase noise with time, and lead to a performance degradation of the parent VCO [16]. Therefore, it can be expected that the overall receiver performance will deteriorate in the presence of the phase noise arising from such a HC effect. In this dissertation, we will analyze the impact of the phase noise arising from the HC effect on the wireless systems built on top of the short-channel MOSFET devices.

1.4 Literature Review

The existing literature has well addressed the impact of the phase noise on the wireless communication transceivers [4, 5, 18-33]. However, none of the phase noise analyses related to the short-channel devices can be found regarding the single-carrier or multi-carrier communications. Moreover, it was clearly pointed out in [30] that the phase noise is crucial for the single-carrier systems since the equalization techniques employed to mitigate the phase noise dominate the hardware costs; the VCO phase noise also plays a key role in the single-carrier time-division multiple-access (TDMA) systems. In [31], the BER degradation has been evaluated as a function of the 3-dB linewidth of the VCO signal's power spectral density for both OFDM and single-carrier systems. In [32], the BER is approximated by the degradation of the signal-to-noise-ratio (SNR) due to the carrier phase jitter. However, such SNR reduction analysis is restricted to the small phase offset range and the corresponding

BER estimate is accurate only for SNR < 10dB and SNR degradation < 0.5 dB [32]. The effect of the VCO phase noise on the error vector magnitude (EVM) of the received signal in the PSK and quadrature amplitude modulation (QAM) systems was discussed according to an artificial statistical model but no VCO circuitry defect was considered in [33].

The influence of phase noise on the OFDM systems has also been comprehensively discussed in the existing literature [4, 5, 18-29]. In [22], the expected SNR reduction has been evaluated accordingly. The expected OFDM SINR decrease induced by the phase noise has been derived in [24]. The error-rate function in terms of common phase errors has been derived in [4]. According to [4, 5, 25, 26], a major problem in OFDM, the intercarrier interference (ICI) has been related to the fluctuation of the *phase noise mask*, which is the *asymptotically averaged power spectral density* (PSD) associated with the VCO's output signal. The phase noise mask addressed in [25, 27-29] has also been adopted as the crucial specification in the European digital terrestrial television broadcasting standards. However, none of the aforementioned phase noise models takes into account the impacts of a variable MOSFET threshold voltage in the presence of hot-carriers for short-channel synchronization devices (in submicron dimension).

Since phase noise is regarded as the most severe cause of OFDM performance degradation [19, 20], the phase noise suppression techniques have been proposed recently [27, 34-36]. ICI self-cancellation coding has been utilized to mitigate the phase noise in [27, 34]. A low-complexity decision-feedback algorithm was developed in [35] to suppress the phase noise. In [36], the least-squares estimation was used to compensate the phase noise induced *common phase error* (CPE) and the ICI. However, none of these approaches considers the HC impact on the OFDM system performance. Although the HC effect on the

OFDM systems has been demonstrated in [37], the suppression of the resulting phase noise was not considered. In the next section, we will clearly point out the contributions by this dissertation work.

1.5 Dissertation Contributions

In this dissertation, we will analyze the phase noise arising from the HCs in the short-channel MOSFET devices on the synchronization circuits for the wireless telecommunication receivers. We will evaluate the synchronization performances of both single-carrier and multi-carrier systems.

In Chapter 2, we will evaluate the impact of the phase noise arising from the short-channel MOSFET devices on the single-carrier wireless systems. In our discussions, we consider the QPSK, 16-QAM and 64-QAM modulations. The topics can be highlighted as follows:

- We utilize a new phase noise model proposed in [38, 39] for the performance evaluation of the wireless single-carrier systems. Then, we derive the exact expected BER performance of the QPSK-based wireless systems built on the short-channel MOSFETs. The expected BER can be specified in terms of the threshold voltage. In addition, we verify our BER formulation via Monte-Carlo simulations.
- The expected BER performance of wireless single-carrier 16-QAM and 64-QAM systems affected by the phase noise arising in the short-channel MOSFETs is provided via the Monte-Carlo simulations.

- The exact expected SINR is derived and then verified via the Monte-Carlo simulations. Our SINR formulation can be employed to predict the SINR performance for the 16-QAM and the 64-QAM systems.
- We provide a new asymptotical BER analysis for the QPSK systems built on the short-channel MOSFET devices. Our new analysis helps validate our expression for the theoretical BER, over the normal MOSFET operating threshold voltage range $0.4 \le V_{th} \le 0.9$. Moreover, our asymptotical BER analysis implies that even with very high transmitter power, the phase noise due to the high MOSFET threshold voltage may cause the system to fail to provide a low target BER.

In Chapter 3, we consider the HC impact on the OFDM-based wireless systems. We provide a new statistical analysis of the phase noise PSD model and make several discoveries, as outlined below:

- We utilize our new phase noise model for the performance evaluation of OFDM systems, and compare the results using the new model with those using the existing phase noise model in [25]. According to our simulation results, we observe a discrepancy up to three orders-of-magnitude in the BER performance between our new phase noise model and the existing one at a nominal SNR of 12 dB. Since the new phase noise model captures the MOSFET device-level imperfections in terms of the threshold voltage increase, our results provide the wireless system designer with the precise information about the expected OFDM system performance, which the existing phase noise model fails to address.
- The SINR formula for the OFDM systems in the presence of phase noise is derived. We show that our SINR formula is applicable for the system performance analysis

when the received SNR is 20 dB or larger, and reason why it is not applicable for the SNRs lesser than 20 dB.

- We quantify the phase noise variance (phase noise power) which results from the MOSFET operating at a particular threshold voltage. In order to achieve this objective, we utilize the knowledge of the offset-frequency limits of the $1/f^2$ region for the phase noise PSD. This phase noise variance expression helps establish a direct link between the MOSFET threshold voltage and the performance of the parent wireless system.
- We show that an increase in the threshold voltage results in an *increased* phase noise power. Consequently, the performance of the parent wireless system also degrades as the threshold voltage increases over time. Thereupon, we demonstrate the expected system performance degradation through our simulations.
- We derive the probability density function (pdf) of the phase noise PSD at a particular offset frequency, by regarding the threshold voltage as a uniformly distributed random variable.
- The average phase noise variance (over all threshold voltages) at a particular offset frequency is formulated in terms of the pdf of the phase noise PSD and the variance at a particular threshold voltage. We then verify this derived average phase noise variance via Monte-Carlo experiments.
- The sensitivity function of the phase noise PSD is also derived. This function helps study the performance of the wireless systems which have been impacted by the phase noise arising from the HC effect.

In Chapter 4, we evaluate the performance of the ICI self-cancellation (SC) coded OFDM in the phase noise induced by the HC effect.

- We find that the ICI self-cancellation coding is very effective for combating the phase noise effects on the OFDM systems.
- We quantify the performance margins that result from the SC-coded OFDM systems in terms of either (i) the SNR margins in dB needed to achieve a target BER, or (ii) the BER improvements operating at a fixed SNR.

1.6 Organization of the Dissertation

This dissertation is organized as follows. Chapter 2 addresses the evaluation of the phase noise impact arising from the HCs on the single-carrier wireless systems. Chapter 3 discusses the phase noise impacts due to the HCs on the OFDM-based wireless systems. Chapter 4 studies the performance of the ICI self-cancellation coded wireless OFDM systems in the presence of the HC-induced phase noise in the short-channel MOSFET devices. Chapter 5 concludes this dissertation.

Chapter 2

Single-Carrier Communication System Performance in the Presence of Phase Noise

2.1 Overview

As we had stated in Chapter 1, the market for high-speed data communication services has opened an era of developing new wireless technologies and standards [8-15]. The explosive growth of the ubiquitous high-speed data networks has led to the burgeoning demand for the compact CMOS devices in the order of submicrons [6, 40]. However, these compact CMOS devices, which are also called the short-channel MOSFET devices, suffer from the hot-carrier (HC) effect which is a major cause of the performance degradation therein [6, 16, 17]. It has also been shown that the HC effect in the MOSFET can enlarge the phase noise with time, and lead to the performance degradation of the parent VCO [16]. Therefore, it can be expected that the overall receiver performance will deteriorate in the presence of the phase noise arising from such an HC effect.

In this chapter, we analyze the impact of the VCO phase noise arising from the HC effect on the performance of any *single-carrier* wireless transceiver built on the short-channel MOSFETs. To the best of our knowledge, there exists no analysis for the impact of the phase noise due to the HC effect on the single-carrier wireless systems. Utilizing the recently-derived phase noise model for the short-channel MOSFETs in [38, 39], we derive the relationships between the system performance in terms of the bit-error-rate (BER) or signal-to-interference-plus-noise ratio (SINR) and the corresponding drifted MOSFET threshold voltage due to the HC effect. In our analysis, we do not use the commonly adopted

assumption $e^{j\theta_n} \approx 1 + j\theta_n$ to restrict on the small phase noise; instead, we derive the exact BER from the precise phase noise model. Consequently, our BER estimate is applicable to all kinds of signal-to-noise ratios (SNRs). To get a better understanding of the phase noise impact due to the HCs on the BER, we investigate the asymptotical BER analysis when the SNR approaches to infinity. We exploit this asymptotic analysis to prove that the BER increases as the MOSFET threshold voltage increases for QPSK and numerically justify the same trend for QAM. Our theoretical analysis and simulations demonstrate that the BER performance of the QPSK systems deteriorates by two orders-of-magnitude at an SNR of 10 dB due to the HC effect while the high-modulation QAM performance is degraded even more severely. We perform the asymptotic BER analysis for high SNR, which implies that even with very high transmitter power the phase noise due to the high MOSFET threshold voltage may still cause the system to fail to achieve a low target BER.

The rest of this chapter is organized as follows. The transmission model for single-carrier systems is described in Section 2.2. The effect of the VCO phase noise on the BER and the SINR is analyzed accordingly in Sections 2.3.1 and 2.3.2 respectively. We derive the exact analytical expression of the BER related to the MOSFET threshold voltage for a single-carrier QPSK system and verify our analytical results through Monte Carlo computer simulations. The simulation results will be presented and discussed in Section 2.4, while Section 2.5 summarizes this chapter.

2.2 Single-Carrier Receiver Model

Throughout this chapter, the subscripts *R* and *I* indicate the real and imaginary parts of the corresponding signals, respectively. Without loss of generality, in order to evaluate the

single-carrier receiver performance solely due to the phase noise effect, we adopt a flat-fading channel model with the additive white Gaussian noise (AWGN) here. The complex envelope $r(t)$ of the received signal in a single-carrier system can be written as [32]:

$$r(t) = \sum_{n=-\infty}^{+\infty} s(n)\, p(t-nT) + w(t), \tag{2.1}$$

where $\{s(n)\}$ is an information symbol sequence randomly and independently drawn from an M-QAM signal constellation [41], $p(t)$ is the pulse-shaping function, T is the symbol period and $w(t)$ represents the complex-valued AWGN with a zero mean and a variance of $2\sigma_w^2$ [41]. The received signal $r(t)$ is fed into the matched filter and then sampled at $t = nT$, which yields the discrete-time signal $r(n) \overset{\Delta}{=} r(nT)$ as given by [32]:

$$\begin{aligned} r(n) &= s(n)e^{j\theta(n)} + w(n) \\ &= \cos\big(\theta(n)\big)s(n) + j\sin\big(\theta(n)\big)s(n) + w(n) \end{aligned}, \tag{2.2}$$

where $\theta(n)$ is the sampled phase noise and $w(n)$ is the AWGN. Assume that the phase noise process $\theta(n)$ is zero-mean Gaussian [22, 42]. For a differential ring oscillator usually found in the VCOs of the wireless communication synchronization devices, the single-sided PSD of the phase noise in terms of the offset frequency (f) is given by [38, 39]:

$$L(f) = \frac{8}{3\eta}\frac{NkT}{P}\left[\frac{\gamma V_{DD}}{\frac{V_{DD}}{2} - V_{th} - \Delta V_{th}} + \frac{V_{DD}}{R_L I_{tail}}\right]\frac{f_0^2}{f^2}, \tag{2.3}$$

where

$$\eta \overset{\Delta}{=} \text{Proportionality constant (=0.75)},$$

$N \overset{\Delta}{=}$ Number of stages in the oscillator (=6),

$k \overset{\Delta}{=}$ Boltzmann's constant (=1.381 x 10^{-23} m^2 kg s^{-2} K^{-1}),

$T \overset{\Delta}{=}$ Absolute temperature (=300K),

$\gamma \overset{\Delta}{=}$ Constant for a short channel device (= 4/3),

$V_{DD} \overset{\Delta}{=}$ Power supply voltage (=3V),

$V_{th} \overset{\Delta}{=}$ Threshold voltage of the CMOS (in volts),

$\Delta V_{th} \overset{\Delta}{=}$ Change in the threshold voltage V_{th} (in volts),

$R_L \overset{\Delta}{=}$ Effective load resistor in one cell (=3KΩ),

$I_{tail} \overset{\Delta}{=}$ Tail current of the differential cell (=0.67mA),

$P \overset{\Delta}{=}$ Power dissipation of the VCO (=10mW),

$f_0 \overset{\Delta}{=}$ Center (carrier) frequency of the VCO (=859 MHz),

$f \overset{\Delta}{=}$ Offset frequency in Hz.

According to [43], the numerical values associated with the parameters in Eq. (2.3) are the typical values and a typical MOSFET *threshold voltage* V_{th} is 0.4 volts [44]. To demonstrate the VCO performance degradation due to the *increased* threshold voltage, we select an upper bound V_{th} = 0.9 volts as the worst case in this work [45]. Figure 2.1 illustrates the phase noise PSD given by Eq. (2.3) with the threshold voltages V_{th} = 0.4, 0.9 volts, respectively.

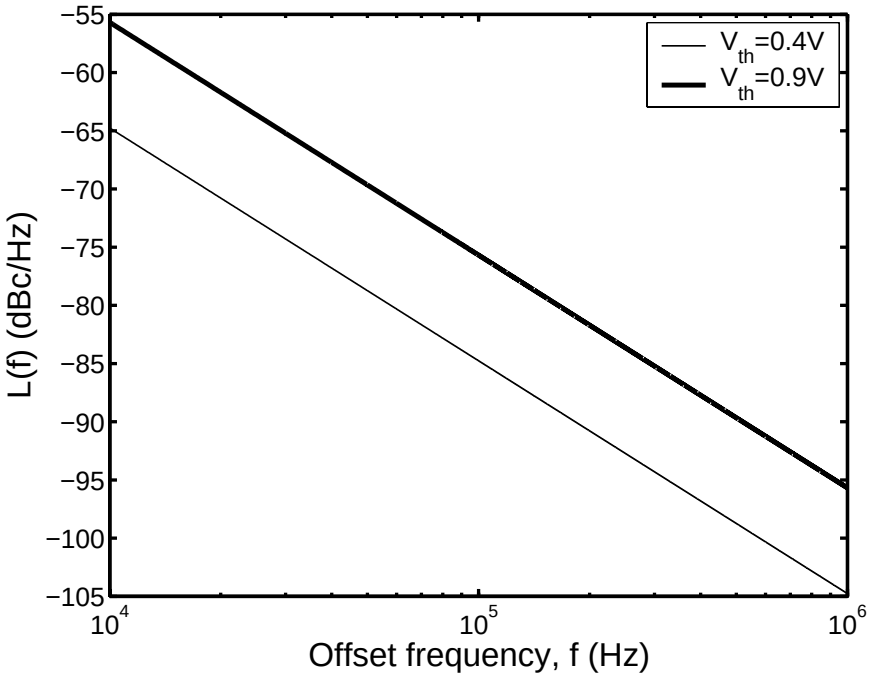

Figure 2.1. Phase noise PSDs for $V_{th} = 0.4$ and $V_{th} = 0.9$ volts.

According to Eq. (2.3) and Figure 2.1, it is noted that the power of the phase noise process in dBc/Hz at each offset frequency (*f*) depends explicitly on V_{th}. Specifically, an increase in the threshold voltage V_{th} results in the increase in the phase noise power at each offset frequency. Thus, the phase noise PSD model given by Eq. (2.3) is a viable tool for evaluating the impact of the phase noise resulting from the HC effect on the wireless systems built on top of the short-channel MOSFET devices.

We can rewrite Eq. (2.2) as

$$\begin{aligned} r_R(n) &\overset{\Delta}{=} s_R(n)\cos\theta_n - s_I(n)\sin\theta_n + w_R(n) \\ r_I(n) &\overset{\Delta}{=} s_I(n)\cos\theta_n + s_R(n)\sin\theta_n + w_I(n) \end{aligned}, \tag{2.4}$$

where the symbol $\theta(n)$ is substituted with θ_n for notational convenience. Eq. (2.4) will be used in the next section for the error performance analysis of a single-carrier receiver in the presence of the HC effect.

2.3 Single-Carrier System Performance

In this section, we will evaluate the BER and the SINR performance of a single-carrier receiver where the phase noise is incurred by the HC effect. We will provide an exact theoretical analysis of the BER for a single-carrier QPSK receiver and verify our derivation with the corresponding Monte Carlo simulations in Section 2.4. For the single-carrier 16-QAM and 64-QAM receivers, we will evaluate the BER performance simply based on the Monte Carlo simulations.

2.3.1 BER Analysis in the Presence of Phase Noise

Consider a single-carrier communication system consisting of information symbols randomly and independently drawn from a QPSK signal constellation $\{\vec{s}_i\}_{1\le i\le 4}$ [8], as shown in Figure 2.2. According to Figure 2.2, it is noted that the most significant bit (MSB) of the phasors $\vec{s}_1$ and $\vec{s}_4$ is zero, while the MSB of the phasors $\vec{s}_2$ and $\vec{s}_3$ is one (unity). Similarly, the least significant bit (LSB) of the phasors $\vec{s}_1$ and $\vec{s}_2$ is zero while the LSB of the phasors $\vec{s}_3$ and $\vec{s}_4$ is one. As illustrated in Figure 2.3, both of the aforementioned MSB and the LSB values can be mapped to the separate horizontal axes [46]. From Figure 2.3(*a*), the probability $P_{V_{th}}$ that the MSB of the received symbol $r(n)$ is incorrectly detected by the receiver at the threshold voltage V_{th} can be derived as [41, 46]:

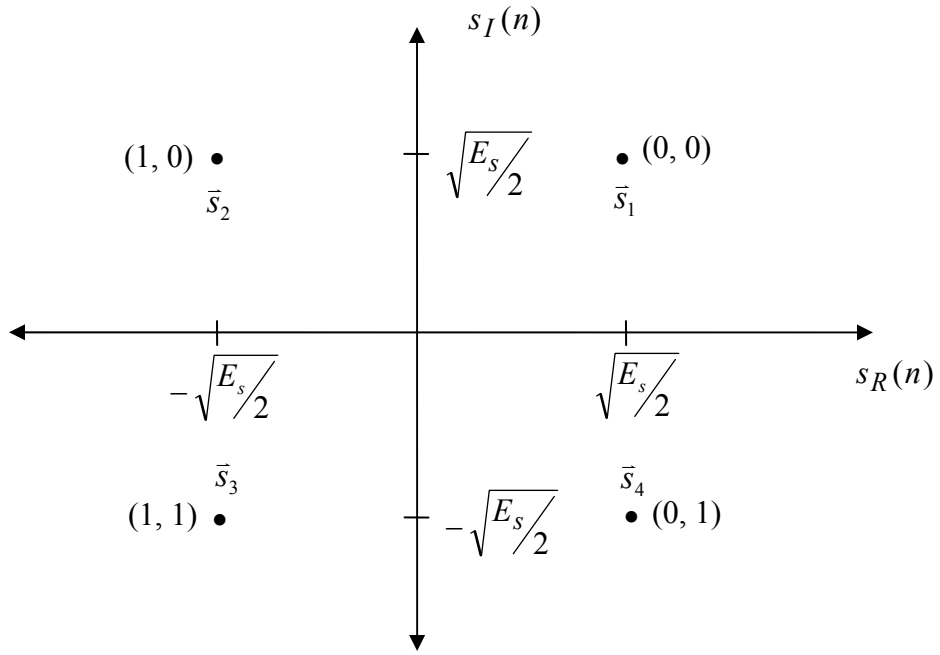

Figure 2.2. A QPSK signal constellation with Gray encoding (E_s is the average symbol energy).

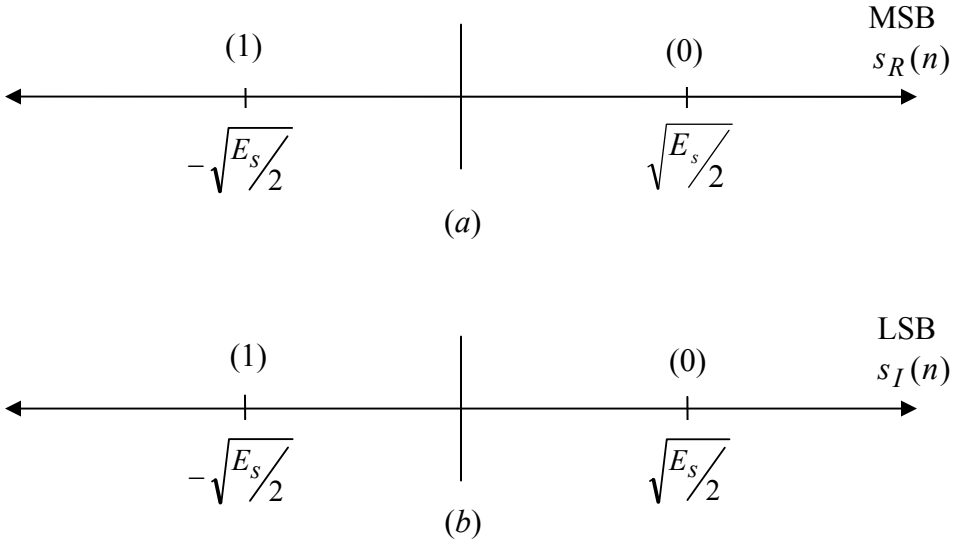

Figure 2.3. Bit allocation pattern for (*a*) MSB and (*b*) LSB in the QPSK signal constellation according to Figure 2.2.

$$\begin{aligned} P_{V_{th}} &= P\left[\varepsilon_{MSB} \mid MSB=0\right] P\left[MSB=0\right] + P\left[\varepsilon_{MSB} \mid MSB=1\right] P\left[MSB=1\right] \\ &= \frac{1}{2} P\left[\varepsilon_{MSB} \mid MSB=0\right] + \frac{1}{2} P\left[\varepsilon_{MSB} \mid MSB=1\right] \end{aligned}, \quad (2.5)$$

where the expression $\varepsilon_{MSB} \mid MSB = i, \quad i = 0,1$, denotes "MSB is detected incorrectly when $MSB = i$ is transmitted", and $P[MSB=0] = P[MSB=1] = 1/2$ [46]. According to Figure 2.2, the probability $P[\varepsilon_{MSB} \mid MSB = 0]$ in Eq. (2.5) can be formulated as

$$\begin{aligned} P\left[\varepsilon_{MSB} \mid MSB=0\right] &= P\left[\varepsilon_{MSB} \mid \vec{s}_1\right] \cdot P(\vec{s}_1) + P\left[\varepsilon_{MSB} \mid \vec{s}_4\right] \cdot P(\vec{s}_4) \\ &= \frac{1}{4} P\left[\varepsilon_{MSB} \mid \vec{s}_1\right] + \frac{1}{4} P\left[\varepsilon_{MSB} \mid \vec{s}_4\right] \end{aligned}, \quad (2.6)$$

where the QPSK symbols $\{\vec{s}_i\}_{1 \le i \le 4}$ are generated equally likely and the expression $\varepsilon_{MSB} \mid \vec{s}_i$ denotes "MSB is detected incorrectly when the symbol $\vec{s}_i$ is transmitted". As shown in Appendix A, $P\left[\varepsilon_{MSB} \mid \vec{s}_1\right]$ in Eq. (2.6) can be derived as

$$P[\varepsilon_{MSB} \mid \vec{s}_1] = \frac{1}{\sqrt{2\pi\lambda^2}} \int_{-\infty}^{+\infty} Q\left[\sqrt{\frac{E_s}{2\sigma_w^2}}\left(\cos\theta_n - \sin\theta_n\right)\right] \exp\left[\frac{-\theta_n^{\,2}}{2\lambda^2}\right] d\theta_n, \quad (2.7)$$

where $\lambda^2 = \lambda^2\left(V_{th}\right)$ is the phase noise variance at the threshold voltage V_{th} and $Q(\cdot)$ is the Gaussian tail probability [41]. Similarly, $P\left[\varepsilon_{MSB} \mid \vec{s}_4\right]$ can be derived as

$$P[\varepsilon_{MSB} \mid \vec{s}_4] = \frac{1}{\sqrt{2\pi\lambda^2}} \int_{-\infty}^{+\infty} Q\left[\sqrt{\frac{E_s}{2\sigma_w^2}}\left(\cos\theta_n + \sin\theta_n\right)\right] \exp\left[\frac{-\theta_n^{\,2}}{2\lambda^2}\right] d\theta_n. \quad (2.8)$$

Then we derive the probability that the MSB of the received symbol $r(n)$ is incorrectly detected at the threshold voltage V_{th} as

$$
\begin{aligned}
P_{V_{th}} &= P[\varepsilon_{MSB} \mid MSB = 0] \\
&= \frac{1}{4\sqrt{2\pi\lambda^2}} \int_{-\infty}^{+\infty} \left\{ Q\left[\sqrt{\frac{E_s}{2\sigma_w^2}} (\cos\theta_n - \sin\theta_n) \right] \right. \\
&\qquad \left. + Q\left[\sqrt{\frac{E_s}{2\sigma_w^2}} (\cos\theta_n + \sin\theta_n) \right] \right\} \exp\left[\frac{-\theta_n{}^2}{2\lambda^2} \right] d\theta_n .
\end{aligned} \tag{2.9}
$$

Since the integrand in Eq. (2.9) is an even function of θ_n, we can rewrite $P_{V_{th}}$ as

$$
\begin{aligned}
P_{V_{th}} = \; & \frac{1}{\sqrt{8\pi\lambda^2}} \int_{0}^{+\infty} \left\{ Q\left[\sqrt{\frac{E_s}{2\sigma_w^2}} (\cos\theta_n - \sin\theta_n) \right] \right. \\
& \left. + Q\left[\sqrt{\frac{E_s}{2\sigma_w^2}} (\cos\theta_n + \sin\theta_n) \right] \right\} \exp\left[\frac{-\theta_n{}^2}{2\lambda^2} \right] d\theta_n .
\end{aligned} \tag{2.10}
$$

The phase noise variance λ^2 can be calculated as [37, 45, 47]:

$$
\lambda^2 = 2 \cdot 10^{\frac{a}{10}} \left[\frac{1}{f_1} - \frac{1}{f_2} \right], \tag{2.11}
$$

where a (in dBc/Hz) is the intercept of the phase noise PSD with the 1 Hz (0 dB) line at the threshold voltage V_{th}; f_1 and f_2 depend on the spectral characteristics of the frequency synthesizer in the radio-frequency (RF) tuner found in the receiver PLL. Moreover, the threshold voltage V_{th} (in volts) can be related to the parameter a (in dBc/Hz) as [37, 45]:

$$
a = 10 \log_{10} \left[\frac{c_1}{K - 2V_{th}} + c_2 \right], \tag{2.12}
$$

where the parameters c_1, c_2 and K are given by $c_1 \overset{\Delta}{=} \frac{8}{3\eta} \frac{NkT}{P} \gamma V_{DD} \frac{f_0^2}{f^2}$,

$c_2 \overset{\Delta}{=} \frac{8}{3\eta} \frac{NkT}{P} \frac{V_{DD}}{R_L I_{tail}} \frac{f_0^2}{f^2}$, $K \overset{\Delta}{=} \frac{V_{DD}}{2} + \varsigma$ and $\varsigma \overset{\Delta}{=} 0.4\,volts$ is the assumed initial

MOSFET threshold voltage. Thus, according to Eqs. (2.11) and (2.12), the relationship between the phase noise variance λ^2 and the threshold voltage V_{th} can be established as

$$\lambda^2 = 2\left(\frac{c_1}{K - 2V_{th}} + c_2\right)\left(\frac{1}{f_1} - \frac{1}{f_2}\right). \tag{2.13}$$

According to Eq. (2.13), the normal threshold voltage range $0.4 \le V_{th} \le 0.9$ will lead to the phase noise range $0 \le \lambda \le 1$. Thereupon, we can express $P_{V_{th}}$ in Eq. (2.10) as $P_M(\lambda) = P_{V_{th}}$, where

$$\begin{aligned} P_M(\lambda) \quad = \quad & \frac{1}{\sqrt{8\pi\lambda^2}} \int_0^{+\infty} \left\{ Q\left[\sqrt{\frac{E_s}{2\sigma_w^2}}\left(\cos\theta_n - \sin\theta_n\right)\right] \right. \\ & \left. + Q\left[\sqrt{\frac{E_s}{2\sigma_w^2}}\left(\cos\theta_n + \sin\theta_n\right)\right] \right\} \exp\left[\frac{-\theta_n^{\,2}}{2\lambda^2}\right] d\theta_n . \end{aligned} \tag{2.14}$$

Similarly, the probability that the LSB of the received symbol $r(n)$ is incorrectly detected at the threshold voltage V_{th}, i.e., $P_L(\lambda)$ can be derived as $P_L(\lambda) = P_M(\lambda)$. Therefore, the overall probability of bit error, or bit-error-rate (BER), $P_b(\lambda)$ for the QPSK system at the threshold voltage V_{th} can be calculated as

$$\begin{aligned} P_b(\lambda) \quad &= \quad P_L(\lambda) + P_M(\lambda) - P_L(\lambda) \cdot P_M(\lambda) \\ &= \quad P_M(\lambda)\left[2 - P_M(\lambda)\right] \end{aligned}, \tag{2.15}$$

where $P_M(\lambda)$ is given by Eq. (2.14). It is noted that the typical values of f_1 and f_2 in Eq. (2.11) are f_1 = 100 Hz, f_2 = 1 MHz [47], and f_1 = 10 KHz, f_2 = 100 KHz [29], based on the specifications of actual frequency synthesizers. In our analysis and in all subsequent simulations, we use f_1 = 5 kHz and f_2 = 1 MHz for illustration [45]. However, we note that the analysis can be extended to other offset frequency ranges in the same manner.

Thus, Eq. (2.15) formulates the theoretical BER performance of a single-carrier QPSK system which has been degraded by the phase noise arising from the HC effect at the threshold voltage V_{th}. In Section 2.3.3, we use an asymptotic analysis to prove that the BER of the QPSK systems as given by Eq. (2.15) increases monotonically as the threshold voltage increases over the normal MOSFET operating range $0.4 \le V_{th} \le 0.9$. Since Eq. (2.14) does not yield the close-form solution, we have to numerically evaluate this expression. We will verify the theoretical BER as given by Eq. (2.15) via computer simulations in Section 2.4.

2.3.2 SINR Analysis in the Presence of Phase Noise

In this section, we will provide the SINR formula for a single-carrier system in which the received signal has been corrupted by the phase noise due to the HC effect. From now on, we assume that the threshold voltage in the VCO MOSFET is V_{th}. According to Eq. (2.2), the received signal $r(n)$ can be written as

$$r(n) = s(n)e^{j\theta_n} + w(n) = s(n) + z(n), \tag{2.16}$$

where $z(n) \overset{\Delta}{=} w(n) + s(n)\left[e^{j\theta_n} - 1\right]$ is the "interference-plus-noise" portion of the received signal. The autocorrelation of the interference-plus-noise random process $\{z(n)\}$ is given by $R_z(n,k) \overset{\Delta}{=} E[z(n)z^*(k)]$, where E is the statistical expectation operator [48]. Since the symbols $\{s(n)\}$ are statistically independent, and $\{w(n)\}$ constitutes the AWGN process, we can derive the variance $\sigma_z^2(V_{th})$ of the process $\{z(n)\}$ as

$$\sigma_z^2(V_{th}) \overset{\Delta}{=} R_z(n,n) = 2\sigma_w^2 + E_s\left[2 - E\left\{e^{j\theta_n} + e^{-j\theta_n}\right\}\right]. \tag{2.17}$$

Using the property $E\left\{e^{j\theta_n}\right\} = E\left\{e^{-j\theta_n}\right\} = e^{-\frac{\lambda^2}{2}}$, where λ^2 is the variance of the phase noise process, we obtain

$$\sigma_z^2(V_{th}) = \sigma_z^2(\lambda) = 2\sigma_w^2 + 2E_s\left[1 - e^{-\frac{\lambda^2}{2}}\right], \tag{2.18}$$

where the variance $\sigma_z^2(V_{th})$ is simply a function of λ and hence we rewrite the variance as $\sigma_z^2(V_{th}) = \sigma_z^2(\lambda)$. Finally, the SINR of the received signal $r(n)$ can be formulated as

$$SINR(\lambda) \overset{\Delta}{=} \frac{E\left\{|s(n)|^2\right\}}{\sigma_z^2(\lambda)} = \frac{E_s}{2\sigma_w^2 + 2E_s\left[1 - \exp\left(-\lambda^2/2\right)\right]}. \tag{2.19}$$

We will verify the theoretical SINR as given by Eq. (2.19) via computer simulations in Section 2.4.

2.3.3 Theoretical Asymptotical BER Analysis Due to the Threshold Voltage in CMOS

In this section, our goal is to perform an asymptotical BER analysis of the QPSK systems. Next, we show that the asymptotical BER function increases monotonically with the increasing threshold voltage in the normal operating range $0.4 \le V_{th} \le 0.9$, i.e.,

$$V_{th}^{(1)} < V_{th}^{(2)} \Rightarrow P_b(\lambda_1) < P_b(\lambda_2), \tag{2.20}$$

where $V_{th}^{(1)}$ and $V_{th}^{(2)}$ are the threshold voltages leading to the variances λ_1^2 and λ_2^2, respectively.

Before deriving the BER as the SNR $\eta \overset{\Delta}{=} \frac{E_s}{\sigma_w^2}$ approaches infinity, we rewrite Eq. (2.14) as

$$P_M(\lambda) = P_M(\eta,\lambda) = \frac{1}{\sqrt{8\pi\lambda^2}} \int_0^{+\infty} \Psi(\eta,\theta_n)\, e^{-\frac{\theta_n^2}{2\lambda^2}}\, d\theta_n, \tag{2.21}$$

where

$$\Psi(\eta,\theta_n) \overset{\Delta}{=} Q\left[\sqrt{\eta}\cos\left(\theta_n + \frac{\pi}{4}\right)\right] + Q\left[\sqrt{\eta}\cos\left(\theta_n - \frac{\pi}{4}\right)\right]. \tag{2.22}$$

We rewrite Eq. (2.21) as

$$P_M(\eta,\lambda) = \frac{1}{\sqrt{8\pi\lambda^2}} \sum_{l=0}^{+\infty} \int_{2l\pi}^{(l+1)2\pi} \Psi(\eta,\theta_n)\, e^{-\frac{\theta_n^2}{2\lambda^2}}\, d\theta_n. \tag{2.23}$$

Notice that in the above equation $\left|\Psi(\eta,\theta_n)\, e^{-\frac{\theta_n^2}{2\lambda^2}}\right| \le 2$. Taking limit $\eta \to \infty$, on both sides of the above equation and then applying the Bounded Convergence Theorem in [49], we get

$$\widetilde{P}_M(\lambda) = \lim_{\eta\to\infty} P_M(\eta,\lambda) = \frac{1}{\sqrt{8\pi\lambda^2}} \sum_{l=0}^{+\infty} \int_{2l\pi}^{(l+1)2\pi} \lim_{\eta\to\infty} \Psi(\eta,\theta_n)\, e^{-\frac{\theta_n^2}{2\lambda^2}}\, d\theta_n. \tag{2.24}$$

For $\theta_n \in [0, 2\pi]$, Eq. (2.22) yields

$$\lim_{\eta\to\infty}\Psi(\eta,\theta_n)=\begin{cases}\dfrac{1}{2}, & \theta_n=\dfrac{\pi}{4}+2l\pi\cup\theta_n=\dfrac{7\pi}{4}+2l\pi\\ 1, & \dfrac{\pi}{4}+2l\pi<\theta_n<\dfrac{3\pi}{4}+2l\pi\cup\dfrac{5\pi}{4}+2l\pi<\theta_n<\dfrac{7\pi}{4}+2l\pi\\ \dfrac{3}{2}, & \theta_n=\dfrac{3\pi}{4}+2l\pi\cup\theta_n=\dfrac{5\pi}{4}+2l\pi\\ 2, & \dfrac{3\pi}{4}+2l\pi<\theta_n<\dfrac{5\pi}{4}+2l\pi\\ 0, & otherwise\end{cases}. \tag{2.25}$$

According to Eqs. (2.24), (2.25), we obtain

$$\widetilde{P}_M(\lambda)=\frac{1}{\sqrt{8\pi\lambda^2}}\sum_{l=0}^{+\infty}\left\{\int_{\beta_{1l}^{+}}^{\beta_{2l}^{-}}e^{-\frac{\theta_n^2}{2\lambda^2}}d\theta_n+2\int_{\beta_{2l}^{+}}^{\beta_{3l}^{-}}e^{-\frac{\theta_n^2}{2\lambda^2}}d\theta_n+\int_{\beta_{3l}^{+}}^{\beta_{4l}^{-}}e^{-\frac{\theta_n^2}{2\lambda^2}}d\theta_n\right\}, \tag{2.26}$$

where $\beta_{1l}\overset{\Delta}{=}\frac{\pi}{4}+2l\pi$, $\beta_{2l}\overset{\Delta}{=}\frac{3\pi}{4}+2l\pi$, $\beta_{3l}\overset{\Delta}{=}\frac{5\pi}{4}+2l\pi$, $\beta_{4l}\overset{\Delta}{=}\frac{7\pi}{4}+2l\pi$. Eq. (2.26) can be reformulated as

$$\begin{aligned}\widetilde{P}_M(\lambda) &= \frac{1}{2}\sum_{l=0}^{+\infty}\left[J_{1l}(\lambda)+2J_{2l}(\lambda)+J_{3l}(\lambda)\right]\\ &= \frac{1}{2}\sum_{l=0}^{+\infty}\left[Q\left(\frac{\beta_{1l}}{\lambda}\right)+Q\left(\frac{\beta_{2l}}{\lambda}\right)-Q\left(\frac{\beta_{3l}}{\lambda}\right)-Q\left(\frac{\beta_{4l}}{\lambda}\right)\right],\end{aligned} \tag{2.27}$$

where $J_{1l}(\lambda)\overset{\Delta}{=}Q\left(\frac{\beta_{1l}}{\lambda}\right)-Q\left(\frac{\beta_{2l}}{\lambda}\right)$, $J_{2l}(\lambda)\overset{\Delta}{=}Q\left(\frac{\beta_{2l}}{\lambda}\right)-Q\left(\frac{\beta_{3l}}{\lambda}\right)$, and $J_{3l}(\lambda)\overset{\Delta}{=}Q\left(\frac{\beta_{3l}}{\lambda}\right)-Q\left(\frac{\beta_{4l}}{\lambda}\right)$. Now we substitute (2.27) into (2.15) and obtain the asymptotic BER as

$$\widetilde{P}_b(\lambda) = \lim_{\eta\to\infty} P_b(\lambda) = \sum_{l=0}^{+\infty}\left[Q\left(\frac{\beta_{1l}}{\lambda}\right)+Q\left(\frac{\beta_{2l}}{\lambda}\right)-Q\left(\frac{\beta_{3l}}{\lambda}\right)-Q\left(\frac{\beta_{4l}}{\lambda}\right)\right] - \frac{1}{4}\left\{\sum_{l=0}^{+\infty}\left[Q\left(\frac{\beta_{1l}}{\lambda}\right)+Q\left(\frac{\beta_{2l}}{\lambda}\right)-Q\left(\frac{\beta_{3l}}{\lambda}\right)-Q\left(\frac{\beta_{4l}}{\lambda}\right)\right]\right\}^2. \tag{2.28}$$

Our next goal is to prove $\widetilde{P}_b(\lambda)$ in (2.28) as a monotonic increasing function of V_{th}. Since $\widetilde{P}_b(\lambda)$ is a monotonic increasing function of $\widetilde{P}_M(\lambda)$, it is sufficient to prove $\widetilde{P}_M(\lambda)$ as a monotonic increasing function of V_{th}. According to Eq. (2.13), we have

$$V_{th}^{(1)} < V_{th}^{(2)} \Rightarrow \lambda_1 < \lambda_2 . \tag{2.29}$$

Thereupon, the asymptotical condition ($\eta \to \infty$) in Eq. (2.20) is equivalent to

$$\lambda_1 < \lambda_2 \Rightarrow \widetilde{P}_b(\lambda_1) < \widetilde{P}_b(\lambda_2),\ 1 \ge \lambda_2 > \lambda_1 \ge 0, \tag{2.30}$$

or

$$\frac{d\widetilde{P}_M(\lambda)}{d\lambda} > 0,\ 0 \le \lambda \le 1. \tag{2.31}$$

We prove in Appendix B that

$$\frac{dJ_{il}(\lambda)}{d\lambda} > 0,\ 0 \le \lambda \le 1,\ i = 1,2,3, \text{ and } l = 0,1,2,\ldots. \tag{2.32}$$

Thus, according to Eqs. (2.29)-(2.32), we get

$$\lambda_1 < \lambda_2 \Rightarrow \widetilde{P}_M(\lambda_1) < \widetilde{P}_M(\lambda_2),\ 1 \ge \lambda_2 > \lambda_1 \ge 0. \tag{2.33}$$

and prove the desired result.

Recall that $0 \le \lambda \le 1$ implies $0.4 \le V_{th} \le 0.9$ which is the regular threshold voltage range of MOSFETs. As illustrated in Figure 2.4 for SNR η=10, 20, 30 dB, the function $\Psi(\eta, \theta_n)$ is very similar to its asymptotical values as given by Eq. (2.25). Our numerical results in the

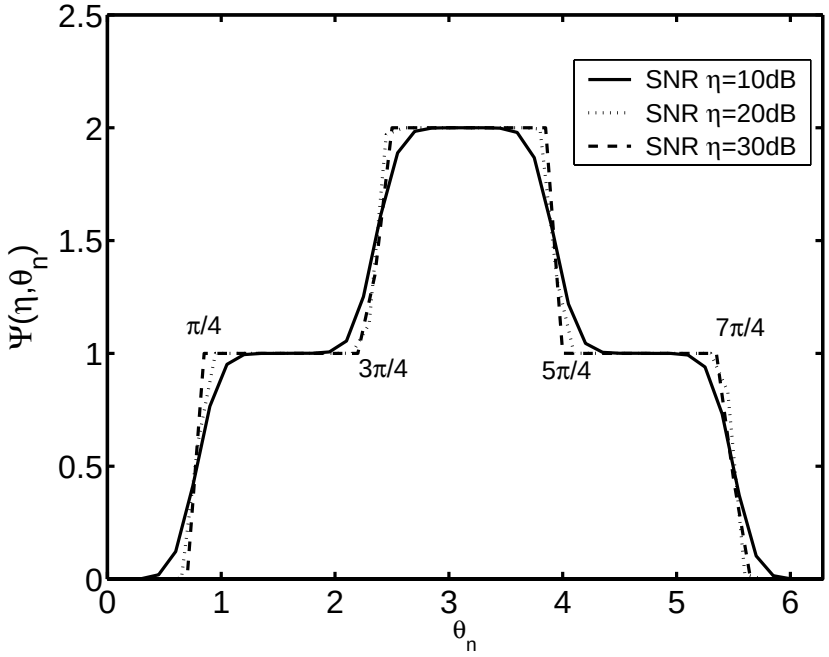

Figure 2.4. Plots of $\Psi(\eta, \theta_n)$ versus θ_n for the range $\theta_n \in [0, 2\pi]$ at SNR=10dB, SNR=20dB and SNR=30dB.

following section demonstrate the monotonic property of BER given by Eq. (2.33) for finite SNR values.

2.4 Simulation Results

In this section, we will verify the theoretical BER analysis given by Eq. (2.15) and the theoretical SINR given by Eq. (2.19) via Monte Carlo simulations. Over different trials, one hundred thousand random QPSK, 16-QAM and 64-QAM symbols are generated and transmitted through an AWGN channel. Perfect timing synchronization is assumed at the receiver. The bit energy E_b is set to unity (i.e., 0 dB) and the variance of the AWGN is assumed to be $\sigma_w^2 = N_0/2$. We choose the two typical values of MOSFET threshold voltages, namely V_{th} = 0.4 volts and V_{th} = 0.9 volts, for illustration [45].

Figure 2.5 depicts the BER performance of a QPSK system which has been degraded by both of the AWGN and the phase noise at the aforementioned threshold voltages. According to Figure 2.5, a close agreement between the theoretical BER given by Eq. (2.15) and the simulated BER appears to be evident. According to Figure 2.5, the single-carrier QPSK system degrades by at least two orders-of-BER-magnitude at a signal-to-noise ratio (E_b/N_0) of 10 dB when the MOSFET threshold voltage increases from V_{th} = 0.4 to V_{th} = 0.9 volts.

Figures 2.6 and 2.7 illustrate the BER performances of a single-carrier 16-QAM system and a 64-QAM system respectively, for the aforementioned threshold voltages. According to Figure 2.6, it is noted that the BER performance of the 16-QAM system deteriorates by two orders-of-magnitude at an SNR of 20 dB when the MOSFET threshold voltage increases from V_{th} = 0.4 volts to V_{th} = 0.9 volts. According to Figure 2.7, the BER performance of the

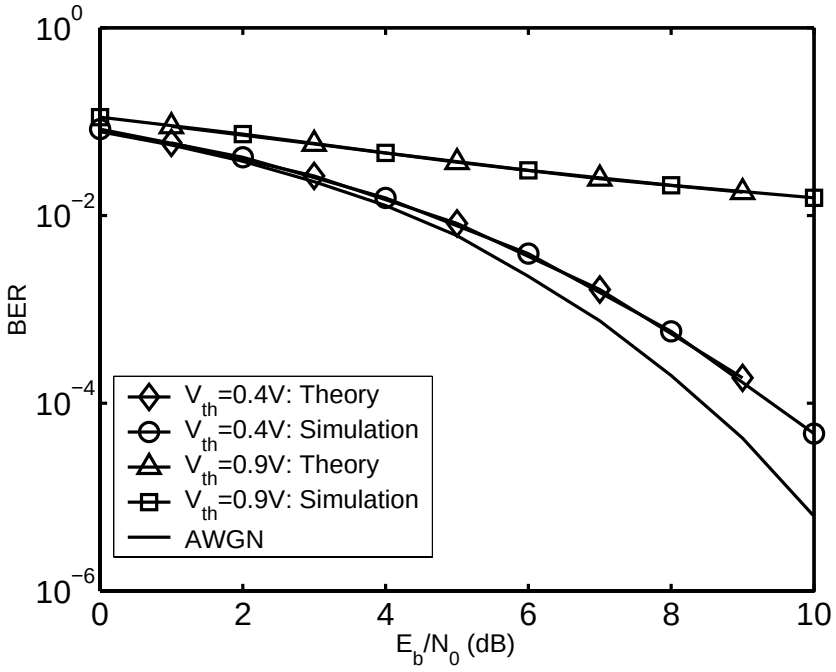

Figure 2.5. BER performance of a single-carrier QPSK system in the presence of phase noise due to the HC effect.

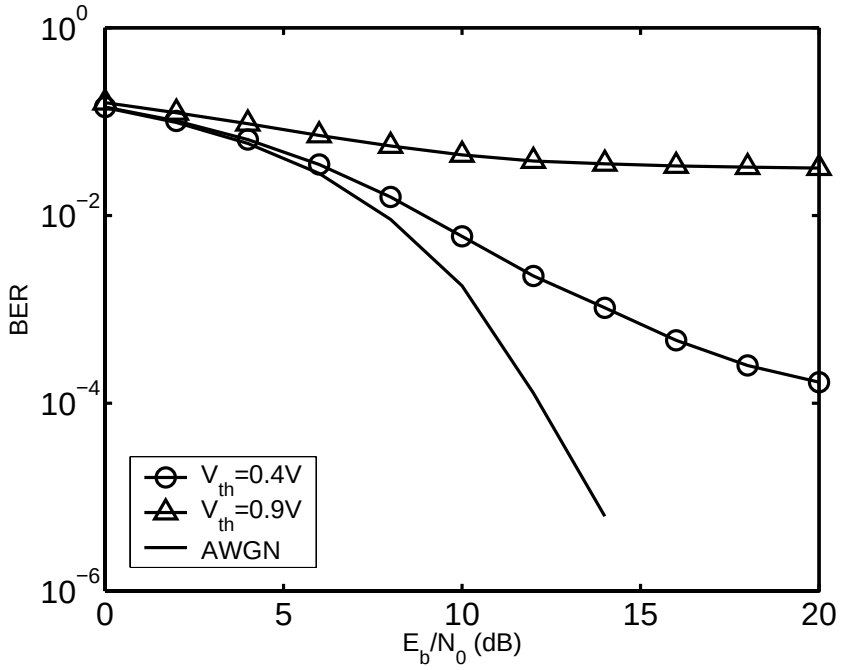

Figure 2.6. BER performance of a single-carrier 16-QAM system in the presence of phase noise due to the HC effect.

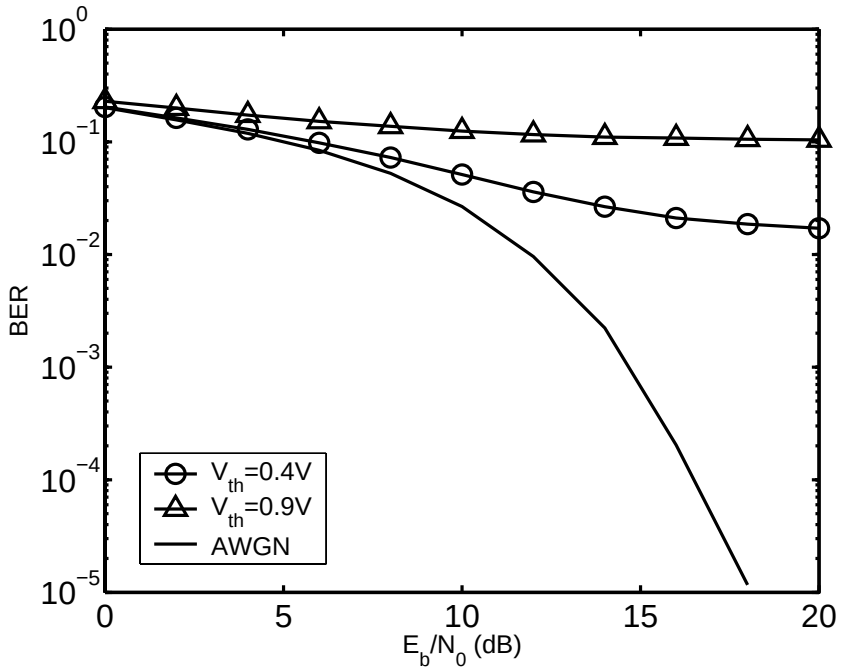

Figure 2.7. BER performance of a single-carrier 64-QAM system in the presence of phase noise due to the HC effect.

64-QAM system degrades by one order-of-magnitude at an SNR of 20 dB when the MOSFET threshold voltage increases from V_{th} = 0.4 volts to V_{th} = 0.9 volts.

According to Figures 2.5-2.7, the 64-QAM systems are more vulnerable to the phase noise arising from the HC effect than the QPSK and 16-QAM systems. It results from that the transmitted signals in single-carrier communication systems undergo a phase rotation due to the phase noise [32], and the higher-order modulation schemes are more sensitive to such subtle changes in the received signal phases than the lower-order modulation schemes [41].

Figure 2.8 depicts the SINR of a QPSK system for V_{th} = 0.4 and 0.9 volts. According to Figure 2.8, it is noted that the theoretical SINR given by Eq. (2.18) closely matches the simulation results for both threshold voltages. Furthermore, from Figure 2.8, it can also be observed that the system SINR degrades by approximately 8 dB at an SNR of 20 dB. Similar

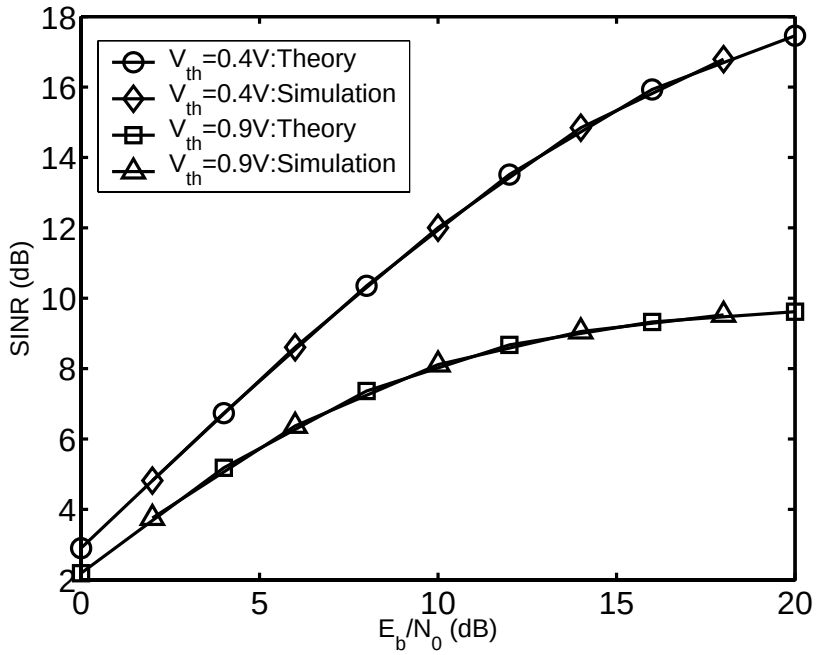

Figure 2.8. SINR performance of a single-carrier QPSK system in the presence of phase noise due to the HC effect.

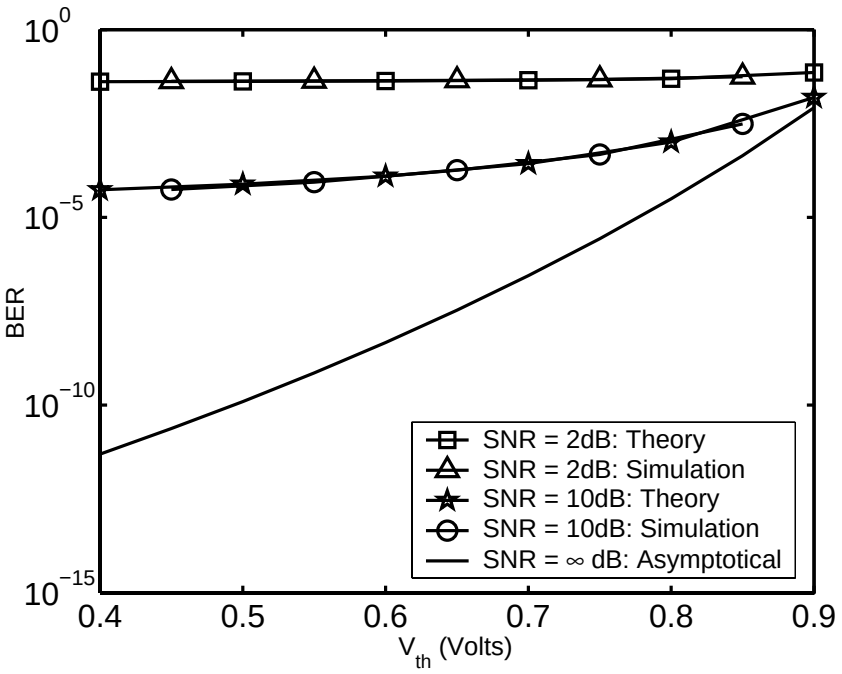

Figure 2.9. BER performance of a single-carrier QPSK system versus the MOSFET threshold voltage V_{th}.

results can be observed for the 16-QAM and 64-QAM systems. Figure 2.9 illustrates the BER degradation of the single-carrier QPSK systems for the threshold voltage range $V_{th} \in$ [0.4, 0.9] at SNR=2dB, 10dB and ∞ dB (asymptotical values). According to Figure 2.9, the theoretical BER given by Eqs. (2.14), (2.15) closely matches the simulated BER for the aforementioned SNR values. Moreover, according to Figure 2.9, it can be noted that the BER of the QPSK systems increases monotonically as a function of the MOSFET threshold voltage V_{th} for the three SNRs, in accordance with our analysis in Sections 2.3.1 and 2.3.3.

According to Figures 2.5-2.9, our asymptotic BER analysis together with Monte Carlo simulations implies that even with very high transmitter power, the phase noise due to high V_{th} (induced by the HC effect) may cause the system to fail to achieve a low target BER.

2.5 Chapter Summary

In this chapter, we evaluated the impact of the phase noise arising from the short-channel MOSFET devices on the single-carrier wireless systems.

We derived the exact expected bit-error-rate (BER) performance of the QPSK-based wireless systems built on the short-channel MOSFETs. In order to derive the exact BER, we did not use the commonly adopted assumption $e^{j\theta_n} \approx 1 + j\theta_n$ to restrict on the small phase noise range; instead, we derive the exact BER from the precise phase noise model. In addition, we verified our BER formulation via the Monte-Carlo simulations. For the 16-QAM- and 64-QAM-based single-carrier systems, the expected BER performance was evaluated using the Monte-Carlo simulations. According to our simulation results, the single-carrier QPSK system performance degrades by at least two orders-of-BER-magnitude at a signal-to-noise ratio (SNR) of 10 dB when the MOSFET threshold voltage increases from V_{th} = 0.4 to V_{th} = 0.9 volts. Over the same threshold voltage range, the BER performance of the 16-QAM system deteriorates by two orders-of-magnitude at an SNR of 20 dB, while the BER performance of the 64-QAM system degrades by one order-of-magnitude at an SNR of 20 dB.

In this chapter we also derived the exact expected signal-to-interference-plus-noise ratio (SINR) and then verified our derived formula via the Monte-Carlo simulations. Our SINR formulation can be employed to predict the exact expected SINR performance for all three types of modulations, namely, QPSK, 16-QAM and the 64-QAM modulations.

In order to validate the expression for the theoretical BER of the QPSK systems affected by the phase noise due to the HC effect, we provide an asymptotical BER analysis. Our

asymptotical BER analysis proves that the BER for the QPSK systems increases monotonically as the MOSFET threshold voltage increases over the normal MOSFET operating threshold voltage range $0.4 \le V_{th} \le 0.9$.

Chapter 3

Phase Noise Impact on the OFDM System Performance

3.1 Overview

As was discussed in Chapters 1 and 2, the wireless communication devices have become an integral part of our daily lives. To support the ever-growing demand for wireless communication devices, OFDM has been adopted as the ubiquitous wireless-access technology [8-12] because it can resist the multipath fading and the impulse noise [51]. However, the phase noise can still remain as a big challenge to OFDM system designers [19, 20]. The phase noise in a VCO's output signal can be modeled as a parasitic phase modulation [22]. This phase modulation occurs on the transmitted and received OFDM signals when the VCO is used as the frequency up- or down-converter [23]. The two major effects of phase noise on the OFDM system performance are a rotation of the signal constellation which gives rise to the *common phase error* (CPE), and *a loss of orthogonality* among subcarriers which induces the *inter-carrier interference* (ICI) [18, 19, 4, 5, 24-29].

In this chapter, we will employ our new phase noise model introduced in Chapter 2 for a more precise OFDM performance analysis based on the HC effect and the drifted threshold voltage [38, 39]. The new phase noise model can be applied for a CMOS differential ring oscillator [43]. We ascertain the impact of the threshold voltage variations on the OFDM system performance and compare our new analysis with that using the existing phase noise model [25]. This chapter is organized as follows. A general introduction to OFDM systems is

presented in Section 3.2. The general OFDM system model and the phase noise effect on the OFDM systems are introduced in Section 3.3. The new phase noise model, the probability density function of the phase noise PSD, the average phase noise variance and the corresponding PSD sensitivity function are derived and discussed in Section 3.4. The OFDM performance evaluation simulations due to the HC effect are presented in Section 3.5. Finally, Section 3.6 will summarize this chapter.

3.2 Introduction to Orthogonal Frequency Division Multiplexing (OFDM)

OFDM is a telecommunication technique in which information-bearing signals with multiple frequencies or *subcarriers*, as shown in Figure 3.1, are transmitted simultaneously

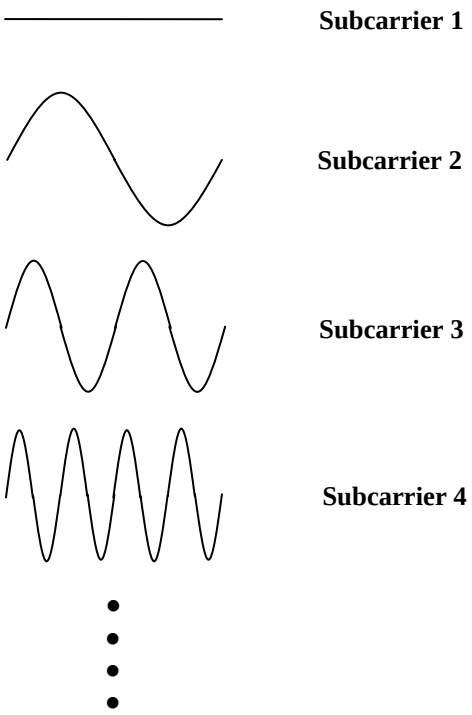

Figure 3.1. Illustration of OFDM subcarriers.

through a communication channel. The *channel* or the medium can be the air in the cases of digital video broadcasting – terrestrial (DVB-T) [8], wireless local area network (WLAN) as described in the IEEE 802.11a and g standards [9, 10], wireless metropolitan area networks (WMANs) based on the IEEE 802.16 family of standards [11], digital audio broadcasting (DAB) [12], or a telephony asymmetrical digital subscriber line (ADSL) [52-55]. Generally speaking, OFDM is also known as *multi-carrier modulation* [47, 51], and the individual information-bearing signals are also commonly known as *subcarriers*.

In the following sections, we will describe the advantages and the challenges associated with the OFDM-based communication systems.

3.2.1 Advantages of OFDM-Based Communications

OFDM-based communication systems possess several advantages which make them a popular candidate for the state-of-the-art and future wireless communication systems. The major advantage of OFDM is that, by virtue of its implementation, the OFDM transceiver experiences a *frequency non-selective* fading channel rather than a *frequency-selective* fading channel as the conventional single-carrier communication systems [51, 56-59]. In frequency-selective fading channels, the *inter-symbol interference* (*ISI*), a well-known problem adversely affects the performance of the conventional *single-carrier* communication systems, while it is thereby mitigated considerably in frequency non-selective fading environments [18, 51, 57-59]. In addition, the *channel estimation* or *equalization* is rather complicated in the single-carrier communication systems [60] but it can easily be implemented with low computational burden in an OFDM transceiver [51]. Furthermore, the linear equalization techniques in the time domain, which are widely used in the single-carrier communications,

are very susceptible to the frequency-selective fadings but they are not needed in OFDM systems [51]. Another advantage of OFDM in practice is that OFDM transceivers can resist the impact of impulse noise commonly occurring in appliances, industrial equipments and automobile engines [51].

3.2.2 Current Challenges Emerging in OFDM Communications

The OFDM mechanism (which will be discussed in detail in Section 3.2.4) would also induce some disadvantages. Some of the major factors to cause the performance degradation of OFDM systems are the *phase noise* resulting from the electronic devices employed in the transmitter and the receiver, the *carrier-frequency offset* and the increased *peak-to-average power ratio* (PAPR) [47]. Carrier-frequency offset (CFO) occurs when the carrier frequencies at the local oscillators have discrepancy among the transmitter and the receiver [18, 61, 62]. In the presence of CFO, the *inter-carrier interference* (ICI) occurs and every subcarrier signal will leak into the neighboring subcarriers to cause the performance degradation [18, 19, 47, 61, 62]. ICI also arises from the high *out-of-band* (OOB) distortion when the instantaneous power of the OFDM waveform swings between high and low values [47]. A large PAPR indicates a very adverse impact of the OOB distortion on the OFDM system performance.

In this dissertation, we will focus on the analysis of the phase noise impact on the OFDM systems. The details will be presented in the Sections 3.2.3, 3.3-3.5 and in Chapter 4.

3.2.3 Phase Noise Impact on the OFDM System Performance in the Presence of Hot-Carriers

As stated in Section 1.3, the HC effect manifests itself as a phenomenon commonly found in electronic circuits and gives rise to the phase noise whose level increases as the operating time progresses. The phase noise, in turn, manifests itself as additional

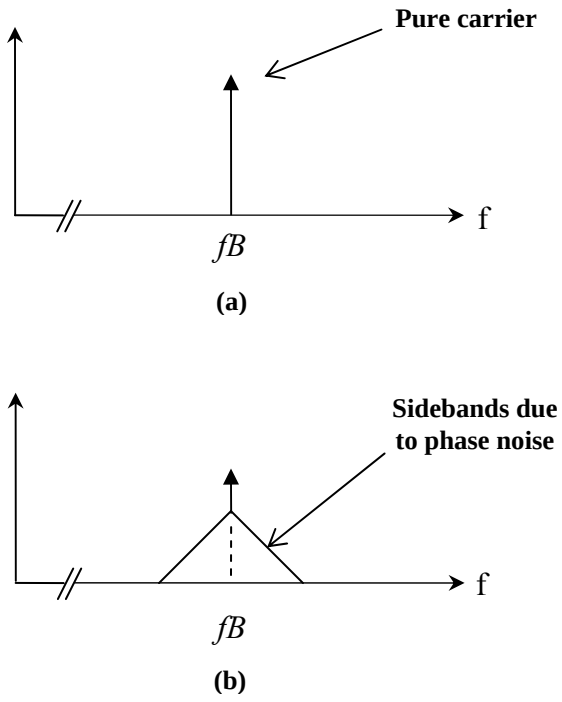

Figure 3.2. The spectra of (a) a pure carrier and (b) a carrier drifted by phase noise.

frequency sidebands on either side of the central (carrier) frequency f_c [6, 16, 17, 38, 39], as illustrated in Figures 3.2a and 3.2b. The phase noise may be regarded as the cause of the most severe performance degradation in OFDM systems [19, 20, 45].

A sinusoidal signal can be represented in the frequency-domain as the *Dirac delta function* such as [63]:

$$\delta(f) \quad = \quad \begin{cases} \infty & , f = 0 \\ 0 & , f \neq 0 \end{cases}, \tag{3.1}$$

where

$$\int_{-\infty}^{\infty} \delta(f)\, df \quad = \quad \int_{0-}^{0+} \delta(f)\, df \quad = \quad 1. \tag{3.2}$$

The additional frequency sidebands cause the ICI, which is depicted in Figure 3.3.

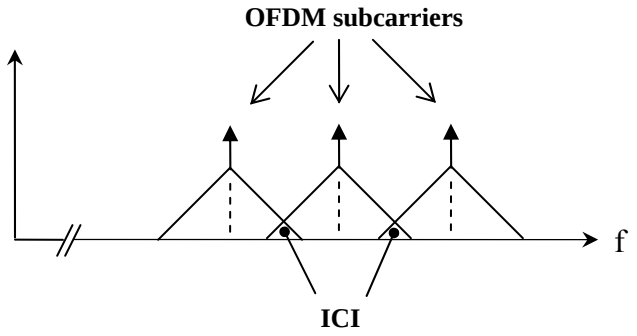

Figure 3.3. Inter-carrier interference (ICI) in OFDM due to phase noise.

In this chapter, we will evaluate the impact of the phase noise arising from the HC effect on the wireless OFDM systems. As will be elaborated in the following chapter, we will employ the threshold voltage V_{th} of the MOSFET device as the parameter which represents the phase noise level caused by the MOSFET. We will then quantify the OFDM system performance in terms of the BER and SINR that result from the phase noise.

3.2.4 OFDM Transceiver Model

The system diagram of a basic OFDM transceiver is depicted in Figure 3.4. The information symbols from a data source are converted into a serial binary stream consisting of information bits. These information bits are then sent to a channel coder which adds redundant bits to combat the subsequent channel distortion. The resulting bit sequence is then

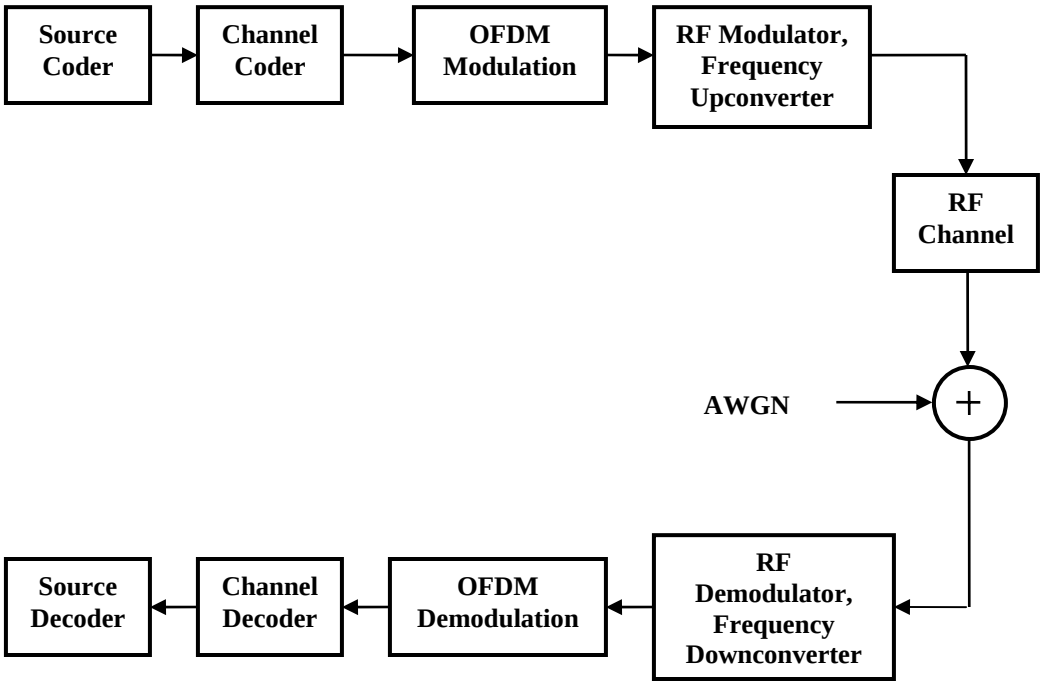

Figure 3.4. Basic OFDM transceiver.

fed to the OFDM modulator, which produces the OFDM symbols. Thereafter, the radio frequency (RF) modulator and the frequency up-converter converts the baseband OFDM signal into the corresponding band-pass signal for the wireless channel. The thermal noise arising from the electronic circuitry is modeled as an additive white Gaussian noise (AWGN) with a variance $N_0/2$ Watts/Hz.

At the receiver, the frequency down-converter transforms the arriving high-frequency signal into the low-frequency baseband signal, and feeds it to the OFDM demodulator. The OFDM demodulator then processes the baseband signal and estimates the transmitted bit sequence. This estimated bit sequence is then sent to the channel decoder, where the redundant bits inserted at the transmitter are removed from the bit stream. Finally, the source decoder recovers the original information symbols.

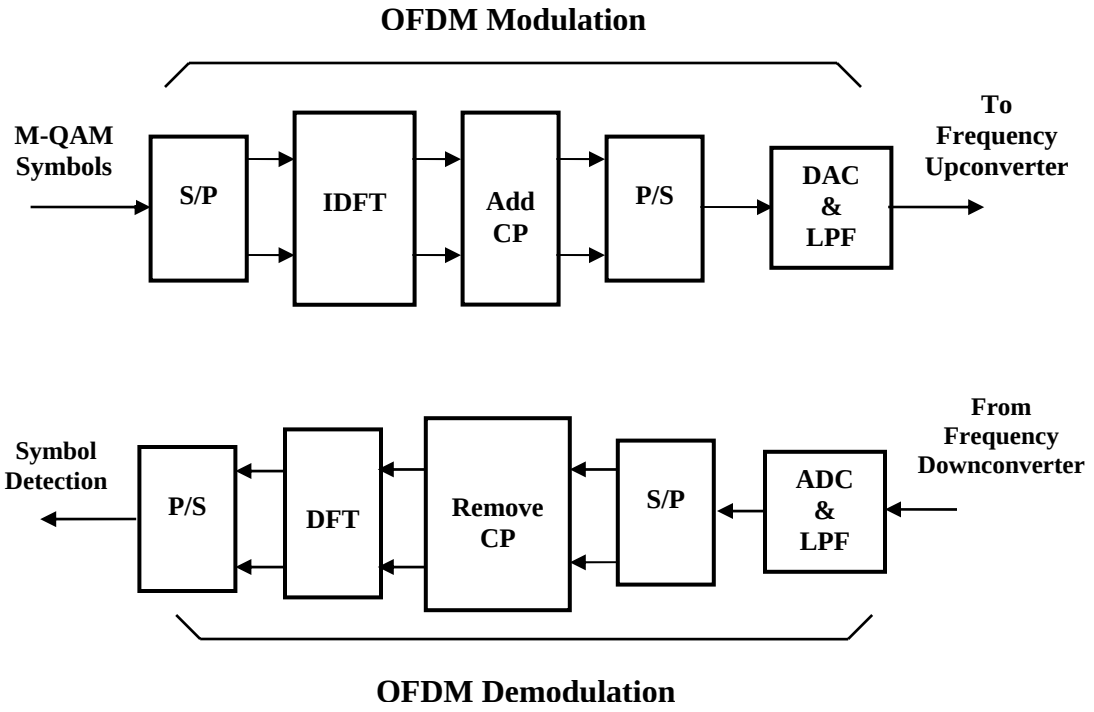

Figure 3.5. OFDM modulation and demodulation sections.

The detailed OFDM modulation and demodulation are both illustrated in Figure 3.5. The output bit stream from the channel coder is first converted into the appropriate complex-valued symbols from an M-QAM signal constellation, for example, the symbols drawn from the 16-QAM as shown in Figure 3.6 [8], where each signal point represents a group of four bits assigned to the respective signal point according to the well-known Gray encoding bit allocation scheme [41].

The complex-valued symbols are then multiplexed into N parallel sub-streams by the serial-to-parallel (S/P) converter. An inverse discrete Fourier transform (IDFT) is then performed on the N symbols, which generates the OFDM symbol consisting of N samples. A cyclic prefix (CP) consisting of a small subset of the N samples from the OFDM symbol is appended to the front of the parent OFDM symbol followed by the parallel-to-serial (P/S)

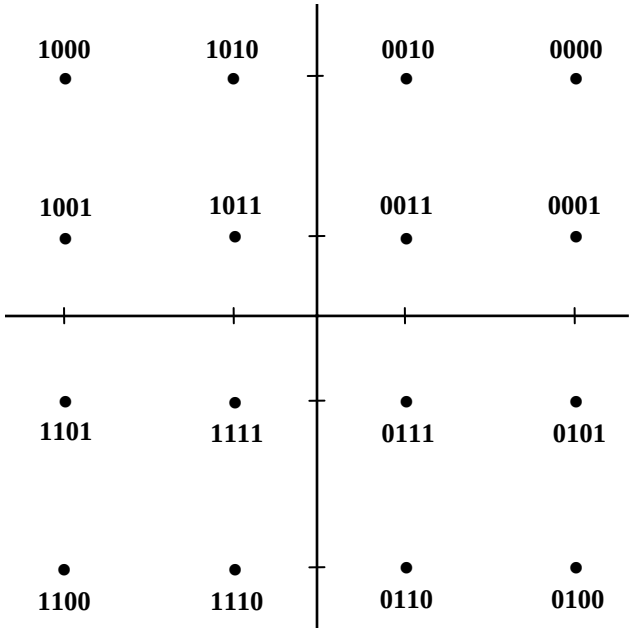

Figure 3.6. Signal constellation of 16-QAM.

converter. The resulting stream can be transformed into a continuous–time baseband signal using both digital-to-analog converter (DAC) and the low-pass filter (LPF). Finally the baseband signal is forwarded to the frequency upconverter for transmission.

At the receiver, the arriving signal will be carried down to form a baseband signal. The down-carried signal will be sent through the corresponding inverse operations of OFDM modulation in the transmitter. Finally the detected bit stream will be generated at the receiver end for the ultimate symbol detection.

3.3 OFDM System Model

In this section, we would like to present the OFDM system model and identify the corresponding phase noise factor. According to this OFDM system model, we can derive the *signal-to-interference-plus-noise ratio* function, which depends on the average phase noise power.

3.3.1 OFDM Signal Model

According to Figure 3.7, the complex envelope of the transmitted OFDM signal with duration T_s, N subcarriers and sampling frequency $f_s = \frac{N}{T_s}$, can be given by [22]:

$$s(n) = \sum_{k=0}^{N-1} a_k \, e^{j\frac{2\pi}{N}kn}, \; n = 0,1,\cdots,N-1, \tag{3.3}$$

where a_k are i. i. d. information symbols drawn from a QPSK or QAM constellation [41]. The transmitted OFDM symbols $s(n)$ are assumed to experience a frequency-flat fading channel with additive white Gaussian noise (AWGN) [22, 27]. The down-converted base-

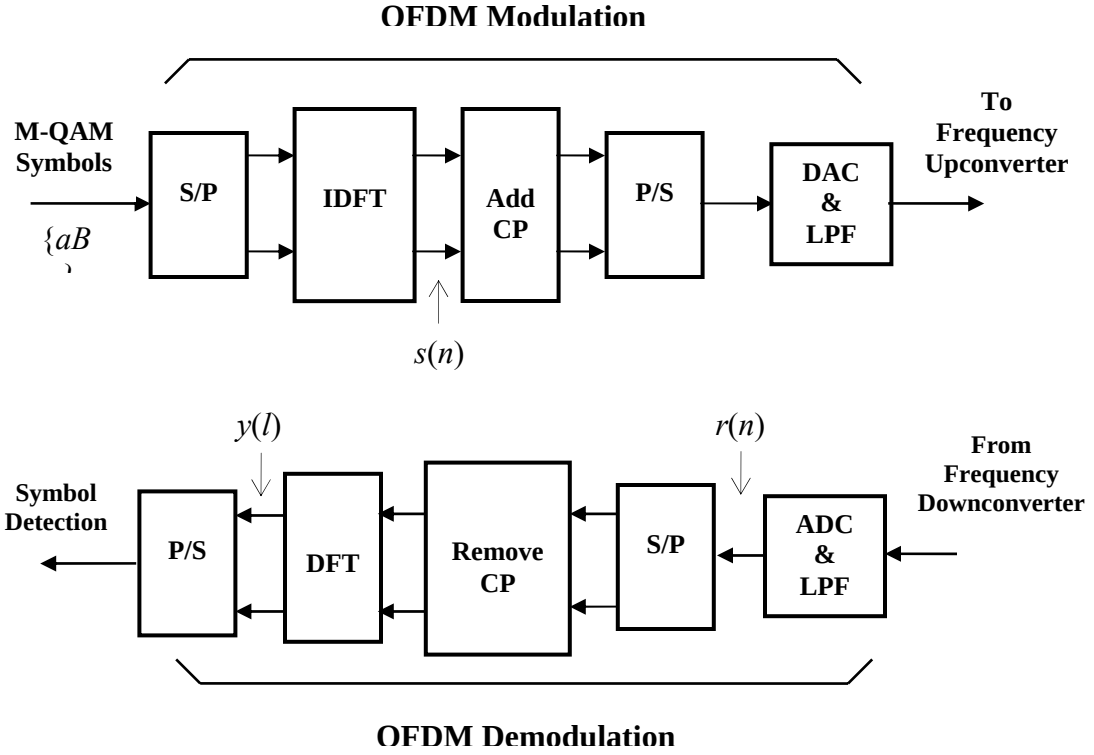

Figure 3.7. OFDM modulation and demodulation sections.

band OFDM signal at the receiver can be formulated as

$$r(n) = s(n)\, e^{j\theta(n)} + v(n)\,, \tag{3.4}$$

where $\theta(n)$ is the sampled zero-mean Gaussian phase noise [22, 42], and $v(n)$ is the zero-mean AWGN with variance $N_0/2$. It is noted that the phase noise process $\theta(n)$ is primarily caused by the synchronization devices, for example, VCOs [16]. Although the phase noise arises from the VCOs in both transmitters and receivers, we just focus on the receiver here for simplicity. As was noted in Section 1.2, the communication circuitry in the transmitter is often much more sophisticated than that in the receiver, and therefore the phase noise induced by the receiver usually is the major concern for the OFDM performance evaluation [4, 5].

The demodulated OFDM signal sequence after the discrete Fourier transform (DFT) can be written as

$$y(l) = \frac{1}{N} \sum_{n=0}^{N-1} r(n)\, e^{-j\frac{2\pi l n}{N}} + w_l\,,\ l = 0,1,\cdots,N-1\,, \tag{3.5}$$

where w_l is the DFT of $\{v(n)\}_{0\le n\le N-1}$. According to [25], we can make the small-angle approximation such that $e^{j\theta(n)} \approx 1 + j\theta(n)$. Thus, the demodulated signal $y(l)$ becomes

$$\begin{aligned} y(l) &\approx \frac{1}{N} \sum_{k=0}^{N-1} a_k \sum_{n=0}^{N-1} e^{j\frac{2\pi}{N}(k-l)n} \\ &\quad + \frac{j}{N} \sum_{k=0}^{N-1} a_k \sum_{n=0}^{N-1} \theta(n)\, e^{j\frac{2\pi}{N}(k-l)n} + w_l \\ &= a_l + e_l + w_l \end{aligned}$$

$$l = 0,1,\cdots,N-1\,, \tag{3.6}$$

where the *demodulation error* e_l is defined as

$$e_l \overset{\Delta}{=} \frac{j}{N} \sum_{\substack{k=0 \\ k \neq l}}^{N-1} a_k \sum_{n=0}^{N-1} \theta(n)\, e^{j\frac{2\pi}{N}(k-l)n}, \; l = 0,1,\cdots,N-1. \tag{3.7}$$

3.3.2 OFDM Demodulation Error Analysis

The demodulation error e_l given by Eq. (3.7) involves two components, namely the *common phase error* (CPE) and the *intercarrier interference* (ICI).

(i) According to Eq. (3.7), when $l=k$, we obtain the CPE as [22]:

$$p_l = \frac{j}{N} a_l \sum_{n=0}^{N-1} \theta(n) = j a_l \Theta, \tag{3.8}$$

where $\Theta \overset{\Delta}{=} \frac{1}{N} \sum_{n=0}^{N-1} \theta(n)$. Eq. (3.8) indicates that all the OFDM subcarriers are rotated by the same angle, Θ radians [4, 5, 22, 24-29].

(ii) According to Eq. (3.7), when $l \neq k$, we can formulate the ICI as [22]:

$$c_l = \frac{j}{N} \sum_{\substack{k=0 \\ k \neq l}}^{N-1} a_k \sum_{n=0}^{N-1} \theta(n)\, e^{j\frac{2\pi}{N}(k-l)n}. \tag{3.9}$$

According to [4, 5, 26], the ICI c_l may be considered as an additive thermal noise, and it approximates a Gaussian process as the number of subcarriers N is large [4, 5, 25, 26].

From Eq. (3.7), we can write e_l as

$$e_l = j \sum_{k=0}^{N-1} a_k \Psi(l-k), \; l = 0,1,\cdots,N-1, \tag{3.10}$$

where $\Psi(l-k)=\frac{1}{N}\sum_{n=0}^{N-1}\theta(n)\,e^{-j\frac{2\pi}{N}(l-k)n}$ is the DFT of the phase noise process $\{\theta(n)\}_{0\le n\le N-1}$ with the subcarrier difference $l-k$. The autocorrelation function of the error process $\{e_l\}$ is given by [48]:

$$\begin{aligned} R_e(l,m) &\overset{\Delta}{=} E(e_l e_m^*) \\ &= \alpha^2 \sum_{k=0}^{N-1} E[\Psi(l-k)\Psi^*(m-k)] \end{aligned}, \tag{3.11}$$

where E is the statistical expectation operator and $\alpha^2 \overset{\Delta}{=} E[|a_l|^2]$ is the average transmitted power. Consequently, the variance $\sigma_e^2(l)$ of the error process $\{e_l\}$ for the l^{th} subcarrier is given by

$$\begin{aligned} \sigma_e^2(l) &\overset{\Delta}{=} E[|e_l|^2] \\ &= \alpha^2 \sum_{k=0}^{N-1} E[|\Psi(l-k)|^2] \end{aligned}, \quad l=0,1,\cdots,N-1, \tag{3.12}$$

and the signal-to-interference-plus-noise ratio (SINR) per subcarrier can be formulated as

$$SINR \overset{\Delta}{=} \frac{\alpha^2}{\frac{1}{N}\sum_{l=0}^{N-1} E[|e_l + w_l|^2]}. \tag{3.13}$$

When $E[|w_l|^2]$ is relatively small to $E[|e_l|^2]$, Eq. (3.13) can be simplified as

$$SINR \approx \frac{\alpha^2}{\frac{1}{N}\sum_{l=0}^{N-1}\sigma_e^2(l)} = \frac{N}{\sum_{l=0}^{N-1}\sum_{k=0}^{N-1}E\left[|\Psi(l-k)|^2\right]} = \frac{1}{\sum_{k=0}^{N-1}E\left[|\Psi(k)|^2\right]} \quad (3.14)$$

According to Eq. (3.14), the SINR per subcarrier is inversely proportional to the phase noise power $\sum_{k=0}^{N-1}E\left[|\Psi(k)|^2\right]$ in the absence of AWGN w_l. This SINR measure will be used for the OFDM system performance evaluation later on.

3.4 Statistical Analysis of the Phase Noise

In the previous section, we showed that the phase noise is a crucial factor to influence the OFDM system performance. In particular, we showed that the OFDM demodulation error can be viewed as being composed of two components, namely the CPE given by Eq. (3.8) and the ICI given by Eq. (3.9). In order to evaluate the impact of the phase noise in statistical terms, we would like to present a new phase noise analysis here, based on the recently derived power spectral density (PSD) model for short-channel MOSFETs [38, 39]. We will then utilize the PSD model to quantify the power of the phase noise process that is generated by the HC effect.

3.4.1 Phase Noise Analysis

For the purpose of our phase noise analysis, we utilize the phase noise power spectral density (PSD) model for a differential ring oscillator described in Chapter 2. For convenience, the expression for the single-sided PSD of the phase noise $\theta(n)$ is repeated below [38, 39]:

$$L(f) = \frac{8}{3\eta}\frac{N\,k\,T}{P}\left[\frac{\gamma\,V_{DD}}{\frac{V_{DD}}{2} - V_{th} - \Delta V_{th}} + \frac{V_{DD}}{R_L\,I_{tail}}\right]\frac{f_0^2}{f^2}, \tag{3.15}$$

where $\eta \triangleq$ Proportionality constant (=0.75), $N \triangleq$ Number of stages in the oscillator (=6), $k \triangleq$ Boltzmann's constant (=1.381 x 10^{-23} m^2 kg s^{-2} K^{-1}), $T \triangleq$ Absolute temperature (=300K), $\gamma \triangleq$ Constant for a short-channel device (= 4/3), $V_{DD} \triangleq$ Power supply voltage (=3V), $V_{th} \triangleq$ Threshold voltage of the CMOS (in volts), $\Delta V_{th} \triangleq$ Change in the threshold voltage V_{th} (in volts), $R_L \triangleq$ Effective load resistance in one cell (=3KΩ), $I_{tail} \triangleq$ Tail current of the differential cell (=0.67mA), $P \triangleq$ Power dissipation of the VCO (=10mW), $f_0 \triangleq$ Center (carrier) frequency of the VCO (=859 MHz), $\triangleq$ Offset frequency (in Hz).

To demonstrate the VCO performance degradation due to the *increased* threshold voltage, we select an upper bound V_{th} = 0.9 volts as the worst case in this work [45]. This PSD given by Eq. (3.15) is also known as *phase noise mask* [4, 5, 47].

According to the phase noise PSD given by Eq. (3.15), the variance σ^2 (in radian^2) of the phase noise is given by [47]:

$$\sigma^2 = \int_{f_1}^{f_2} 2L(f)\,df\,, \tag{3.16}$$

where the integration limits f_1 and f_2 depend on the spectral characteristics of the frequency synthesizer in the radio-frequency tuner. Typical values are f_1 = 10 kHz, f_2 = 100 kHz [29], and f_1 = 100 Hz, f_2 = 1 MHz [47], based on the specifications of actual frequency synthesizers.

According to [23], the conventionally approximated phase noise PSD $L(f)$ (in dBc/Hz) is a function of the offset frequency f (in dBHz) given by

$$L(f) = a + b\,f\,, \tag{3.17}$$

where a (in dBc/Hz) is the intercept of the phase noise PSD function with the 1 Hz (0 dBHz) line, and b (in dB/decade) is the slope of the phase noise PSD function. According to the new phase noise PSD model as given by Eq. (3.15), b = -20 dB/decade can be derived as shown in Figure 2.1. Table 3.1 lists the values of a that correspond to the selected threshold

Table 3.1. Typical a values for the new phase noise PSD model

Threshold voltage (V_{th}) (volts)	a **(dBc/Hz)**
0.5	15.88
0.6	16.72
0.7	17.91
0.8	19.85
0.9	24.32

voltage values in the range of $0.5 \le V_{th} \le 0.9$. According to Figure 2.1 and Table 3.1, it is noted that the different intercepts a resulting from different threshold voltages V_{th} will obviously change the phase noise PSD function $L(f)$. *Therefore, we discover that the phase noise PSD model should vary with respect to the threshold voltage in the short-channel MOSFETs.*

According to Eq. (3.17), we obtain the phase noise PSD in (Watts/Hz) as a function of both threshold voltage V_{th} and offset frequency f as

$$L(f, V_{th}) = 10^{0.1a'} \cdot f^{0.1b}, \tag{3.18}$$

where a' is the intercept of the phase noise PSD function with the 1 Hz (0 dBHz) line at the threshold voltage V_{th} and f is now expressed in Hz. Based on our model, the phase noise variance (in rad^2) at the threshold voltage V_{th} can then be calculated within the frequency range $[f_1, f_2]$ as

$$\sigma^2(a') = 2 \cdot 10^{\frac{a'}{10}} \left[\frac{1}{f_1} - \frac{1}{f_2} \right]. \tag{3.19}$$

In our analysis and all simulations in this chapter, we choose f_1 = 10 kHz and f_2 = 1 MHz for illustration. However, as was noted in Chapter 2, this analysis may be easily extended to other frequency ranges in the same manner.

3.4.2 Probability Density Function of the Phase Noise PSD

According to the analysis in Section 3.4.1, the phase noise PSD is a function of the random threshold voltage V_{th} for a fixed offset frequency f. Thus, according to Eq. (3.15)

together with a constant f, we have

$$L(V_{th}) = K_1 \left[\frac{K_2}{K_5 - V_{th} - \Delta V_{th}} + K_3 \right] K_4, \tag{3.20}$$

where

$$\begin{aligned} K_1 &\stackrel{\Delta}{=} \frac{8}{3\eta} \frac{N k T}{P} \\ K_2 &\stackrel{\Delta}{=} \gamma V_{DD} \\ K_3 &\stackrel{\Delta}{=} \frac{V_{DD}}{R_L I_{tail}} \\ K_4 &\stackrel{\Delta}{=} \frac{f_0^2}{f^2} \\ K_5 &\stackrel{\Delta}{=} \frac{V_{DD}}{2} \end{aligned} .$$

This yields

$$L(V_{th}) = \frac{c_1}{K - 2V_{th}} + c_2, \tag{3.21}$$

where

$$\begin{aligned} c_1 &\stackrel{\Delta}{=} K_1 K_2 K_4 \\ c_2 &\stackrel{\Delta}{=} K_1 K_3 K_4 . \\ K &\stackrel{\Delta}{=} K_5 + \varsigma_1 \end{aligned}$$

Assuming that V_{th} is *uniformly* distributed within the range $[\varsigma_1, \varsigma_2]$, we derive the probability density function (pdf) of the phase noise PSD $L(V_{th})$ for any fixed f. Since the threshold voltage V_{th} is random, the spectral density coefficient $L(V_{th})$ is therefore also random and we can simplify such a random variable as $l \stackrel{\Delta}{=} L(V_{th})$ for notational

convenience. Thus, the pdf $p_L(l)$ of the phase noise PSD can be obtained as

$$p_L(l) = \begin{cases} \dfrac{c_1}{2(\varsigma_2 - \varsigma_1)(l - c_2)^2} & , \; c_2 + \dfrac{c_1}{K - 2\varsigma_1} \le l \\ & \cup \quad l \le c_2 + \dfrac{c_1}{K - 2\varsigma_2} \quad , \\ 0 & , \quad otherwise \end{cases} \tag{3.22}$$

where

$$c_1 \overset{\Delta}{=} \frac{8}{3\eta} \frac{N k T}{P} \gamma V_{DD} \frac{f_0^2}{f^2}$$

$$c_2 \overset{\Delta}{=} \frac{8}{3\eta} \frac{N k T}{P} \frac{V_{DD}}{R_L I_{tail}} \frac{f_0^2}{f^2}.$$

$$K \overset{\Delta}{=} \frac{V_{DD}}{2} + \varsigma_1$$

According to Eq. (3.22) and the typical numerical parameters given by Eq. (3.15), Figure 3.8 depicts the pdf of the phase noise PSD at an offset frequency f = 10 kHz on a logarithm scale. From Figure 3.8, it is noted that the phase noise PSD would involve the uncertainty between $l = -65$ dBc/Hz and $l = -55$ dBc/Hz but appear to be -65 dBc/Hz most likely. Similar analyses can be found for different offset frequencies.

3.4.3 Average Phase Noise Variance

According to Eq. (3.19), the phase noise variance is a function of a', where a' is the intercept of the phase noise PSD function with the 1 Hz (0 dBHz) line at the threshold voltage V_{th}. Assuming that V_{th} is uniformly distributed within the range [ς_1, ς_2], we derive the average variance of the phase noise over the offset frequency range [f_1, f_2]. Since the

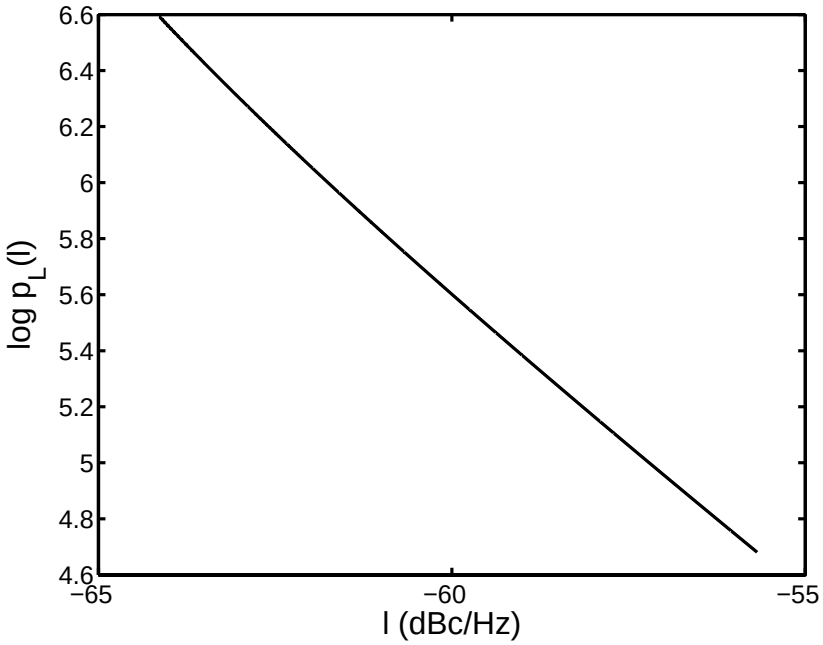

Figure 3.8. Probability density function of the phase noise PSD at f = 10 kHz.

threshold voltage V_{th} is random, the intercept a' is therefore also random. According to Eqs. (3.19) and (3.22), the average phase noise variance $\overline{\sigma}^2$ (in rad^2) can then be obtained as

$$\overline{\sigma}^2 = \int_{l_1}^{l_2} \sigma^2(a)\, p_L(a)\, da\,, \tag{3.23}$$

where $p_L(a)$ is the pdf of the phase noise PSD at the offset frequency f = 1 Hz, and

$$l_1 \overset{\Delta}{=} c_2 + \frac{c_1}{K - 2\varsigma_1}$$

$$l_2 \overset{\Delta}{=} c_2 + \frac{c_1}{K - 2\varsigma_2}$$

are the upper and lower integral limits of the phase noise PSD at the offset frequency f = 1 Hz, for the given threshold voltage V_{th}. In this case, c_1, c_2 and K are given by

$$c_1 \stackrel{\Delta}{=} \frac{8}{3\eta}\frac{NkT}{P}\gamma V_{DD} f_0^2$$

$$c_2 \stackrel{\Delta}{=} \frac{8}{3\eta}\frac{NkT}{P}\frac{V_{DD}}{R_L I_{tail}} f_0^2 .$$

$$K \stackrel{\Delta}{=} \frac{V_{DD}}{2} + \varsigma_1$$

According to Eq. (3.23), the average phase noise variance (in rad^2) over the offset frequency range $[f_1, f_2]$ when V_{th} is uniformly distributed within the range $[\varsigma_1, \varsigma_2]$ can be derived as

$$\overline{\sigma}^2 = \left\{\frac{c_1}{\varsigma_2 - \varsigma_2}\left(\frac{f_2 - f_1}{f_1 f_2}\right)\right\} \cdot \left\{\log_e \frac{|l_2 - c_2|}{|l_1 - c_2|} - \frac{c_2 (l_1 - l_2)}{(l_1 - c_2)(l_2 - c_2)}\right\} . \quad (3.24)$$

Table 3.2 lists the average phase noise variances $\overline{\sigma}^2$ calculated from Eq. (3.24) (theoretical) and from the Monte Carlo simulations over the frequency ranges of actual frequency synthesizers in [4, 29, 47]. For illustration, we choose f_1 = 1 kHz, f_2 = 200 kHz [4], f_1 = 10 kHz, f_2 = 100 kHz [29], and f_1 = 100 Hz, f_2 = 1 MHz [47]. According to

Table 3.2. Theoretical and simulation values of the average phase noise variance $\overline{\sigma}^2$

OFFSET FREQUENCY RANGE $[f_1, f_2]$	THEORETICAL $\overline{\sigma}^2$ (RAD^2)	SIMULATION $\overline{\sigma}^2$ (RAD^2)
[1 KHZ, 200 KHZ]	**0.1437**	**0.1449**
[10 KHZ, 100 KHZ]	**0.013**	**0.013**
[100 HZ, 1 MHZ]	**1.4445**	**1.4449**

Table 3.2, there is a close agreement between our derived theoretical values for $\overline{\sigma}^2$ as given by Eq. (3.24) and the corresponding values obtained from the simulations.

Thus, since the phase noise variance σ^2 quantifies the impact of the phase noise on the OFDM system performance [22, 27, 28], Eq. (3.24) can be used to predict the performance of an OFDM system in the presence of the phase noise arising from the hot-carrier effect. Furthermore, since the sampled phase noise $\theta(n)$ is assumed to be zero-mean, the phase noise variance σ^2 is equivalent to the phase noise power. Therefore, Eq. (3.24) can also be applied to estimate the expected signal-to-interference-plus-noise ratio (SINR) according to Eq. (3.14) for the OFDM systems.

3.4.4 Sensitivity Analysis of Phase Noise PSD

According to Eq. (3.15), the sensitivity function $S(V_{th})$ of the phase noise PSD can be defined as the ratio of the change in the PSD, namely $dL(f)$, with respect to the change in the threshold voltage dV_{th} at a particular offset frequency, i.e. $S(V_{th}) \triangleq \frac{dL(f)}{dV_{th}}$. Consequently, we derive the sensitivity function as

$$S(V_{th}) = \frac{2\lambda}{(g - 2V_{th})^2}, \tag{3.25}$$

where

$$\lambda \triangleq \frac{8}{3\eta}\frac{NkT}{P}\gamma V_{DD}\frac{f_0^2}{f^2},$$
$$g \triangleq \frac{V_{DD}}{2} + \varsigma_1$$

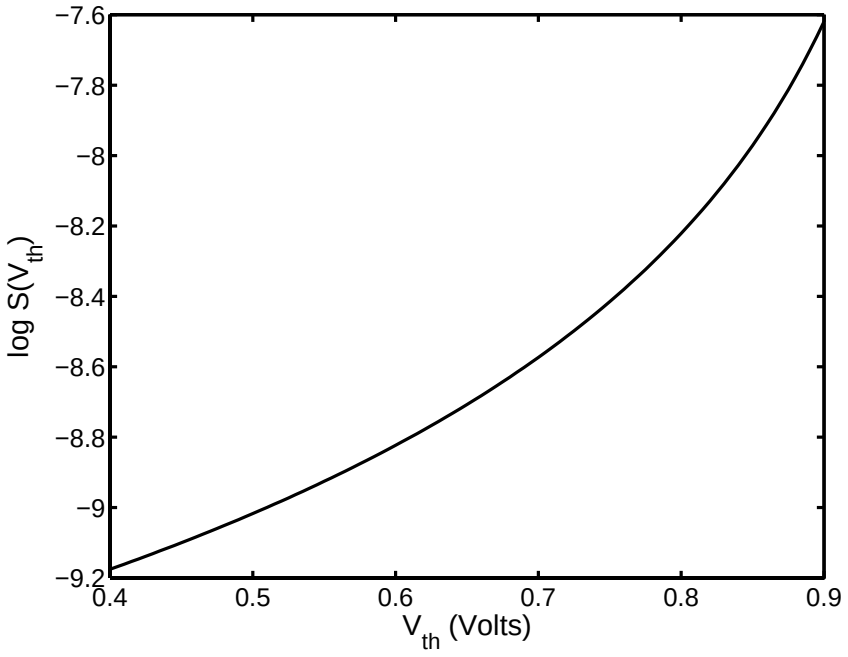

Figure 3.9. Sensitivity of the phase noise PSD at the offset frequency f =1MHz.

and ς_1 is the lower limit of the threshold voltage. Figure 3.9 depicts the sensitivity function $S(V_{th})$ on a logarithm scale at an offset frequency f = 1 MHz. According to Eq. (3.25) and the typical numerical parameters given by Eq. (3.15), we illustrate the sensitivity function $S(V_{th})$ in Figure 3.9, where the sensitivity of the phase noise PSD increases as the threshold voltage increases. In the next section, we will utilize our derived sensitivity function $S(V_{th})$ to study the OFDM performance in the presence of the hot-carriers.

3.5 Simulation Results

We provide simulations here to compare our new phase noise analysis as described in the previous sections with the existing analysis in [25]. The existing phase noise model in [25] for our comparison can be given by

$$L(f) = 10^{-c''} + \begin{cases} 10^{-a''} & , \quad |f| \le f_1 \\ 10^{-(f-f_1)\frac{b''}{f_2 - f_1} - a''} & , \quad f_1 < f \\ 10^{(f+f_1)\frac{b''}{f_2 - f_1} - a''} & , \quad f < -f_1 \end{cases} \quad , \tag{3.26}$$

where the parameters a'' and f_1 determine the characteristics of the phase-locked loop (PLL), b'' determines the slope of the corresponding phase noise PSD, and the parameters c'' and f_2 determine the noise floor. In addition, we chose the minimum threshold voltage ς_1=0.4 volts and the maximum threshold voltage ς_2=0.9 volts for our model. Since no information about the VCO CMOS threshold voltage in [25] is available [64], the median value (V_{th} = 0.65 volts) is chosen to generate the PSD model in this work. Figure 3.10 illustrates the phase noise PSD functions that correspond to the aforementioned threshold

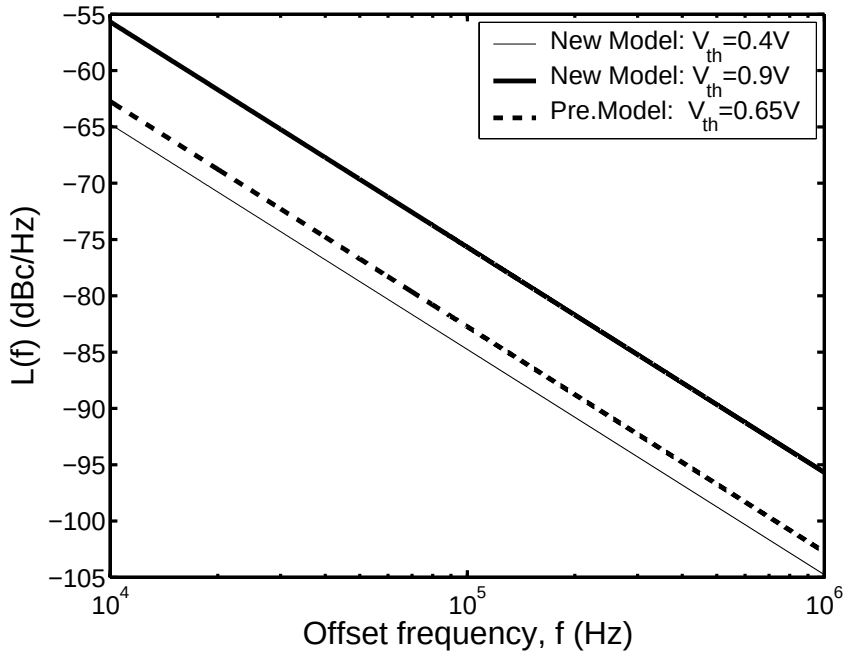

Figure 3.10. Power spectral density functions from the new and previous phase noise models.

Table 3.3. Phase noise variances σ^2 for the new and the previous phase noise models

NEW PHASE NOISE MODEL (V_{TH} = 0.4 VOLTS)	NEW PHASE NOISE MODEL (V_{TH} = 0.9 VOLTS)	PREVIOUS PHASE NOISE MODEL [25] (V_{TH} = 0.65 VOLTS, ASSUMED)
0.013 RAD^2	**0.107 RAD^2**	**0.02 RAD^2**

voltages, while Table 3.3 lists the corresponding phase noise variances for the offset frequency range [10 kHz, 1 MHz].

Monte Carlo simulations were carried out for one hundred thousand random QPSK-OFDM, 16-QAM-OFDM and 64-QAM-OFDM symbols transmitted over an AWGN channel. In our experiments, no phase error correction scheme was used to improve the receiver performance. It is also assumed that the frequency offset does not exist. The number of subcarriers N was chosen as 128.

Figures 3.11-3.13 present the bit-error-rate (BER) performance of the QPSK-OFDM, 16-QAM-OFDM and 64-QAM-OFDM systems respectively for various threshold voltages (V_{th}=0.4, 0.65, 0.9 volts). It is noted that the 64-QAM-OFDM system yields the most severely degraded performance due to the phase noise, while the QPSK-OFDM is least sensitive to the subtle threshold voltage increases. According to Figure 3.9, it is noted that the sensitivity of the phase noise PSD *increases* at higher threshold voltages. The higher the threshold voltage, the higher the phase noise power as given by Eq. (3.16). The higher-order QAM systems are usually more sensitive to the phase noise power than the lower-order QAM and QPSK systems [27].

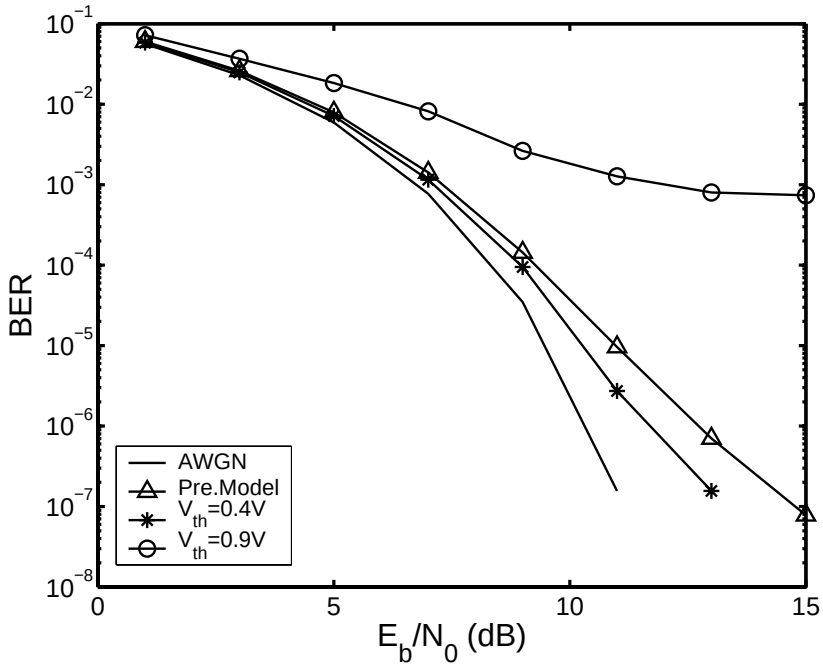

Figure 3.11. BER Performance of QPSK-OFDM, N=128.

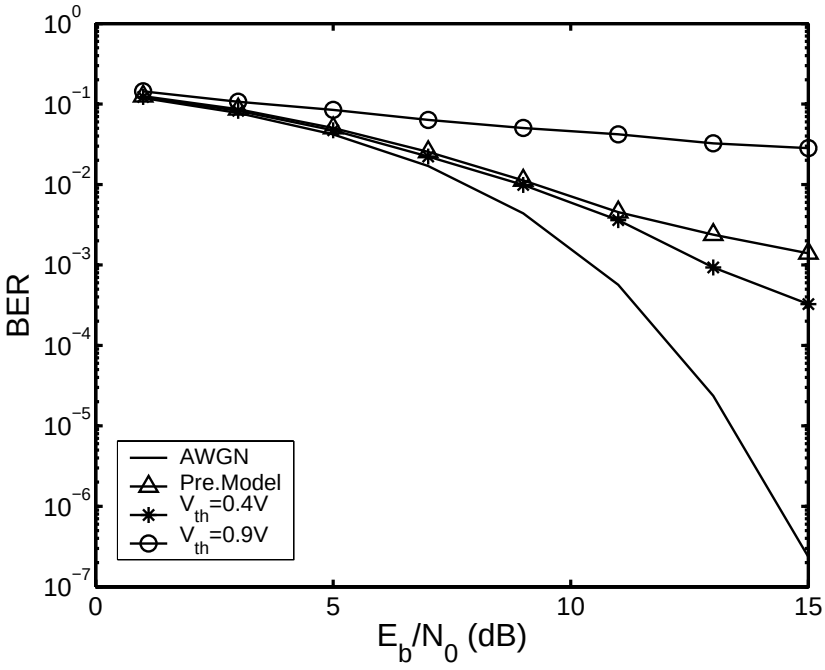

Figure 3.12. BER Performance of 16QAM-OFDM, N=128.

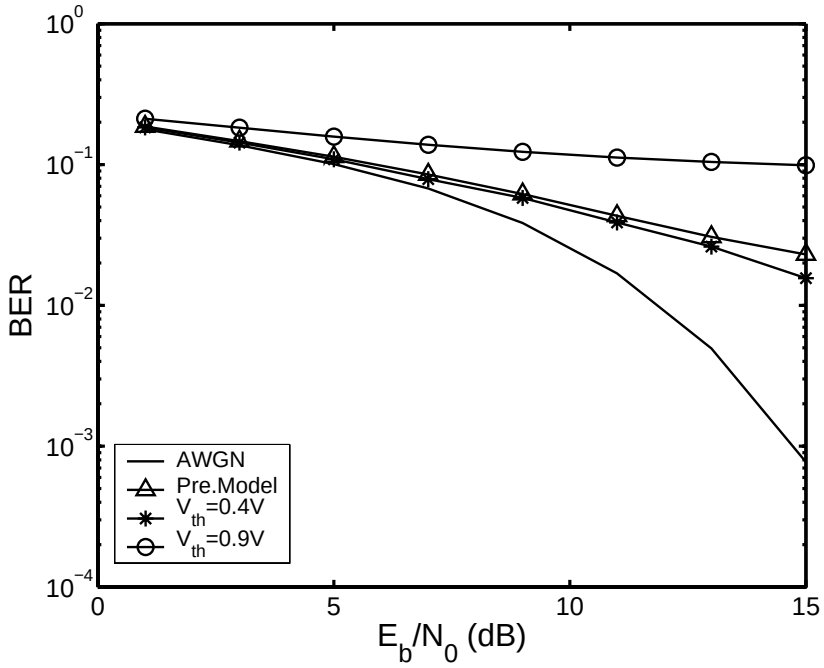

Figure 3.13. BER Performance of 64QAM-OFDM, N=128.

From Figures 3.11-3.13, we observe an obvious discrepancy of three orders-of-magnitude in the BER performance between our new phase noise model and the existing one in [25] at a nominal signal-to-noise ratio (SNR= E_b / N_0) of 12 dB. According to Figures 3.11-3.13, it is observed that a BER floor occurs at the threshold voltages close to V_{th} = 0.9 volts when the SNR values are larger than 12 dB. At the threshold voltages close to V_{th} = 0.9 volts, the condition $\sigma^2|_{V_{th}=0.9V} >> (N_0/2)|_{12\,dB}$ for the phase noise power exists and therefore the phase noise power σ^2 dominates over the channel noise variance $N_0/2$. In addition, for large subcarrier numbers N, the phase noise is the major cause of the ICI [4, 5]. Since the ICI affects the OFDM systems similar to the channel noise [4, 5], the BER floor as depicted in Figures 3.11-3.13 can be found, which is contributed by the constant phase noise power.

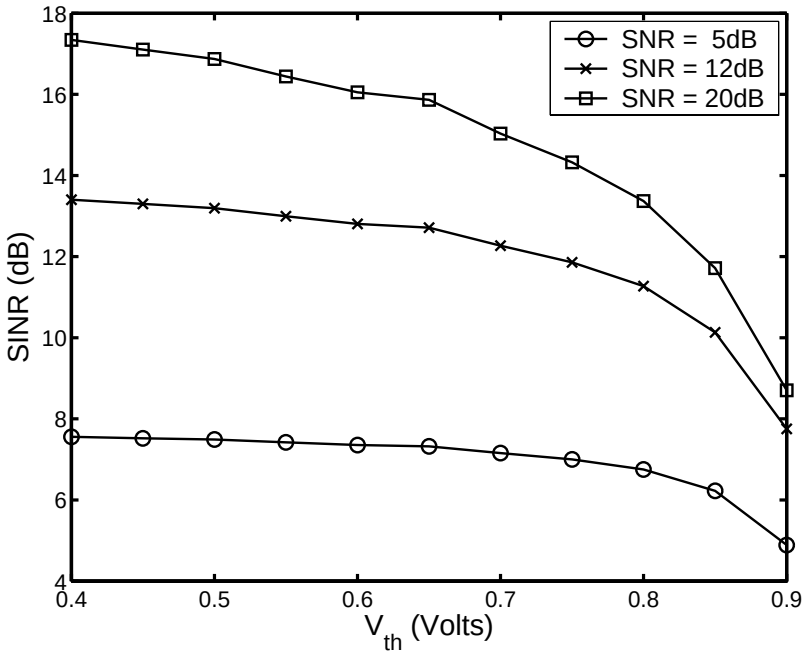

Figure. 3.14. Signal-to-interference-plus-noise ratio (SINR) performance of QPSK-OFDM.

Figure 3.14 illustrates the signal-to-interference-plus-noise ratio (SINR) per subcarrier as a function of the threshold voltage, V_{th}, for the QPSK-OFDM system. According to Figure 3.14, the SINR is reduced by 9 dB when the threshold voltage varies from 0.4 to 0.9 volts at the SNR = 20 dB. It is noted that when the SNR is 20 dB, the SINR degrades *throughout* the range $V_{th} \in$ [0.4V, 0.9V]. Over this range of the threshold voltage, the phase noise dominates the channel noise. Therefore, the simplified SINR measure in Eq. (3.14) is valid in such an SNR. In addition, according to Figure 3.9, the sensitivity of the phase noise mask *increases* at high threshold voltages. This suggests that a rapid decrease in SINR would be expected at high V_{th} values when the SNR is 20 dB.

According to Figure 3.14, when the SNR is 5dB, the SINR is nearly constant for $V_{th} \in$ [0.4V, 0.65V] and then deteriorates for $V_{th} \in$ [0.65V, 0.9V]. In the former range of the

threshold voltage, the constant channel noise dominates the phase noise while in the latter case both channel noise and phase noise are large enough to affect the SINR performance. Similar results can be found for the 16QAM-OFDM and the 64-QAM-OFDM systems. Empirically speaking, the simplified SINR model in Eq. (3.14) is appropriate when the SNR is larger than 15 dB and our phase noise analysis presented in this work is the major focus for the OFDM system evaluation.

3.6 Chapter Summary

In this chapter, we employed a new phase noise model for the performance evaluation of OFDM systems, and we compared our results using the new model in [38, 39] with the results using the existing phase noise model in [25]. We selected V_{th} = 0.4 volts as the nominal initial threshold voltage of the MOSFET devices employed in our VCO, and V_{th} = 0.9 volts as the upper limit of the operating threshold voltage. We then evaluated the performance of the OFDM system built on top of the MOSFET devices with these parametric values by means of Monte-Carlo simulations.

According to our simulation results, we observed a discrepancy of three orders-of-magnitude in the BER performance between our new phase noise model and the existing one at a nominal signal-to-noise ratio (SNR) of 12 dB. Since the new phase noise model captures the MOSFET device-level imperfections in terms of the threshold voltage increase, our results provide the wireless system designer with precise information about the expected OFDM system performance while the existing phase noise analysis provides no such information.

We demonstrated the expected OFDM system performance degradation through our simulation results in terms of the bit-error-rate (BER) and the signal-to-interference-plus-noise ratio (SINR). According to our simulation results, the 64-QAM-OFDM systems yield the most severely degraded BER performance while the QPSK-OFDM systems are least sensitive to the subtle threshold voltage variations. Moreover, we showed that the SINR for QPSK-, 16-QAM- and 64-QAM-OFDM systems is reduced by 9 dB when the threshold voltage varies from 0.4 to 0.9 volts at the SNR = 20 dB.

In this chapter, we also derived the probability density function (pdf) of the phase noise PSD at a particular offset frequency, and then utilized the pdf to evaluate the average phase noise variance at this particular offset frequency.

The sensitivity function of the phase noise PSD, defined as the ratio of the incremental change in the phase noise power at a particular offset frequency to the corresponding change in the threshold voltage was also derived. This function helps explain the performance of the parent wireless systems which have been impacted by the phase noise arising from the HC effect.

Chapter 4

OFDM System Enhancement Using ICI Self-Cancellation Coding

4.1 Overview

As discussed in Chapter 3, the intercarrier interference (ICI) is a crucial problem incurred in the practical OFDM systems. The ICI usually arises from the phase noise in the local VCO, the carrier frequency offset (CFO), and the time synchronization errors in the demodulator. The ICI can degrade the OFDM receiver performance. Consequently, for the quality-of-service (QoS) assessment, it is essential to study the hot carrier (HC) effect and mitigate the associated phase noise or ICI. In this chapter, we investigate a means, ICI self-cancellation coding, for the OFDM system enhancement by eliminating the ICI [27, 61, 62]. Through our simulations, we quantify the performance margin of the ICI self-cancellation coded (SC-coded) OFDM system over the plain OFDM system. We discover that the ICI self-cancellation coding is very effective for combating the HC-induced phase noise. Moreover, the SC-coded OFDM system is also cost-effective since the ICI self-canceller is implemented as a simple differential decoder [18, 61, 62].

This chapter is organized as follows: Section 4.2 discusses the general OFDM system model according to [27]. Section 4.3 introduces the phase noise analysis and Section 4.4 presents the simulation results. The summary will be provided in Section 4.5.

4.2 ICI Self-Cancellation Coded OFDM System Model

The SC-coded OFDM transceiver is illustrated in Figure 4.1 according to [27, 61]. The primary difference between the conventional OFDM transceiver as depicted in Figure 3.5 and the SC-coded OFDM transceiver is that for the latter an ICI self-cancellation encoder is inserted between the serial-to-parallel (S/P) block and the inverse discrete Fourier transform (IDFT) block in the OFDM transmitter. Similarly, an ICI self-cancellation decoder is inserted between the discrete Fourier transform (DFT) and the parallel-to-serial (P/S) blocks in the SC-coded OFDM receiver. The ICI self-cancellation coding for the information symbols d_m is carried out as follows [27, 61, 62]:

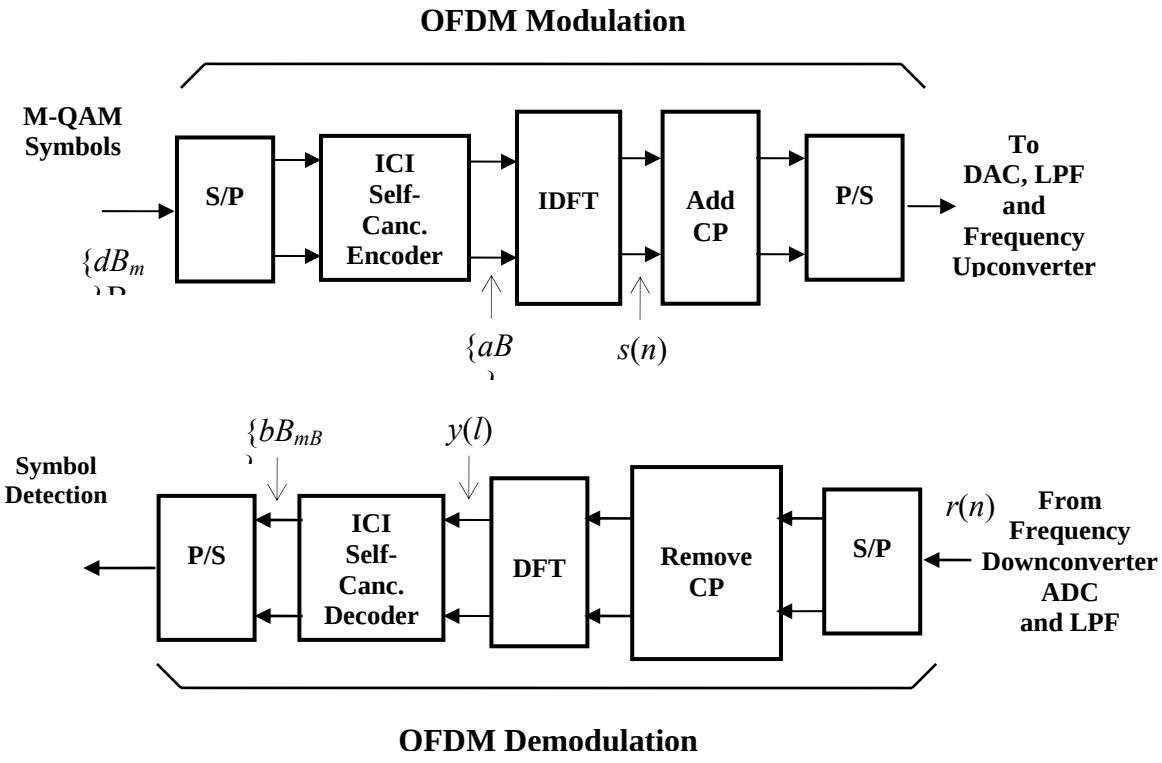

Figure 4.1 ICI self-cancellation coded OFDM transceiver.

$$d_m = a_{2m} = -a_{2m+1},\ m = 0,1,\cdots,\frac{N}{2}-1. \tag{4.1}$$

The complex envelope of the transmitted OFDM signal with duration T_s, subcarrier number N and sampling frequency $f_s = N/T_s$, is given by [21]:

$$s(n) = \sum_{k=0}^{N-1} a_k\, e^{j(2\pi/N)kn},\ n = 0,1,\cdots,N-1, \tag{4.2}$$

where a_k are either the SC-coded symbols resulting from Eq. (4.1) or the ordinary QAM or QPSK symbols. The transmitted OFDM symbols $s(n)$ are assumed to experience frequency-flat fading with additive white Gaussian noise (AWGN) having zero-mean and variance $N_0/2$. The frequency down-converted (base-band) OFDM signal at the receiver can be formulated as [21]:

$$r(n) = s(n)\, e^{j\theta(n)} + v(n), \tag{4.3}$$

where $\theta(n)$ is the zero-mean Gaussian phase noise [22, 42], and $v(n)$ is the zero-mean AWGN with variance $N_0/2$.

As we stated in Sections 1.2 and 3.3.1, the phase noise arises from the VCOs in both transmitter and receiver. However, we only consider the receiver here for simplicity since the phase noise induced by the receiver usually causes the major degradation of the OFDM performance.

Disregarding the AWGN term, the demodulated OFDM signal sequence after the DFT can be written as

$$y(l) = \frac{1}{N}\sum_{n=0}^{N-1} r(n)\, e^{-j\frac{2\pi ln}{N}}$$
$$= \frac{1}{N}\sum_{n=0}^{N-1}\left\{\sum_{k=0}^{N-1} a_k\, e^{j\frac{2\pi(k-l)n}{N}}\right\}.e^{j\theta(n)} \quad , l = 0,1,\cdots,N-1. \tag{4.4}$$

According to Eq. (4.1), the $2m^{\text{th}}$ demodulated subcarrier sequence can be written as

$$y_{2m} = \frac{1}{N}\sum_{L=0}^{\frac{N}{2}-1} d_L \sum_{n=0}^{N-1}\left(e^{j\frac{4\pi n(L-m)}{N}} - e^{j\frac{2\pi n[2(L-m)+1]}{N}}\right).e^{j\theta(n)}, \tag{4.5}$$

where $m = 0,1,\cdots,\frac{N}{2}-1$. Furthermore, let's denote

$$\Psi_p \equiv \frac{1}{N}\sum_{n=0}^{N-1} e^{j\theta(n)}\, e^{-j\frac{2\pi np}{N}}, \tag{4.6}$$

where $p = -(N-1),\cdots,0,\cdots,N-1$. Note that Ψ_p is the DFT of $e^{j\theta(n)}$. Thus, we can rewrite Eq. (4.5) as

$$y_{2m} = d_m\,[\Psi_0 - \Psi_{-1}] + \sum_{\substack{L=0 \\ L\neq m}}^{\frac{N}{2}-1} d_L\,[\Psi_{2(m-L)} - \Psi_{2(m-L)-1}], \tag{4.7}$$

where $m = 0,1,\cdots,\frac{N}{2}-1$. Similarly, the $(2m+1)^{\text{th}}$ demodulated subcarrier sequence is given by

$$y_{2m+1} = d_m\,[\Psi_1 - \Psi_0] + \sum_{\substack{L=0 \\ L\neq m}}^{\frac{N}{2}-1} d_L\,[\Psi_{2(m-L)+1} - \Psi_{2(m-L)}], \tag{4.8}$$

where $m = 0,1,\cdots,\frac{N}{2}-1$. The ICI self-cancellation decoding operation is given by [27]:

$$b_m = \frac{y_{2m} - y_{2m+1}}{2}, \quad m = 0,1,\cdots,\frac{N}{2}-1. \tag{4.9}$$

Substitution of Eqs. (4.7) and (4.8) into Eq. (4.9) yields

$$\begin{aligned} b_m = d_m &+ \frac{1}{2} d_m[-\Psi_{-1} + 2(\Psi_0 - 1) - \Psi_1] \\ &+ \frac{1}{2} \sum_{\substack{L=0 \\ L \neq m}}^{\frac{N}{2}-1} d_L[-\Psi_{2(m-L)+1} + 2\Psi_{2(m-L)} - \Psi_{2(m-L)-1}] \end{aligned}, \tag{4.10}$$

where $m = 0,1,\cdots,\frac{N}{2}-1$. The first term d_m in Eq. (4.10) is the subject signal and the second term $\frac{1}{2} d_m[-\Psi_{-1} + 2(\Psi_0 - 1) - \Psi_1]$ is the common phase error (CPE) while the third term $\frac{1}{2} \sum_{\substack{L=0 \\ L \neq m}}^{\frac{N}{2}-1} d_L[-\Psi_{2(m-L)+1} + 2\Psi_{2(m-L)} - \Psi_{2(m-L)-1}]$ is the ICI induced by the phase noise.

Ψ_p may be considered as the *sampled* power spectral density (PSD) of the phase noise process $\theta(n)$. According to Eq. (4.10), it is noted that the ICI induced by the phase noise can be completely cancelled for those samples of Ψ_p which appear to have a linear relationship with p [27]. This phenomenon is utilized in [27, 34] for the mitigation of general phase noise in OFDM systems. We will apply the same principle for the ICI cancellation, where the ICI is induced by the hot carriers instead. The details will be shown in Sections 4.3 and 4.4.

4.3 Phase Noise Analysis

The phase noise variance (in rad^2) resulting from the phase noise PSD model in Eq. (3.15) can be calculated within the offset frequency range $[f_1, f_2]$ as [23, 37, 45]:

$$\sigma^2 = 2 \cdot 10^{\frac{a}{10}} \left[\frac{1}{f_1} - \frac{1}{f_2} \right], \tag{4.11}$$

where a (in dBc/Hz) is the intercept of the phase noise mask with the 1 Hz (0 dB) line. In the analysis and simulations provided in this chapter, we will use f_1 = 10 kHz and f_2 = 1 MHz for illustration. Table 4.1 lists the values of the phase noise variances which result from Eq. (4.11) for the threshold voltage $0.5 \le V_{th} \le 0.9$ of interest. From Table 4.1, we have found that the higher threshold voltages correspond to the higher phase noise variance values.

Figure 4.2 depicts the average amplitude $|\Psi_p|$ in the logarithm scale for the threshold voltages V_{th} = 0.7 volts and V_{th} = 0.9 volts. Note that most $|\Psi_p|$ values (except those close to

Table 4.1. Phase noise variances for different threshold voltages

Threshold Voltage (V_{th}) (Volts)	**Phase Noise Variance (rad^2)**
0.5	0.01
0.6	0.01
0.7	0.01
0.8	0.02
0.9	0.05

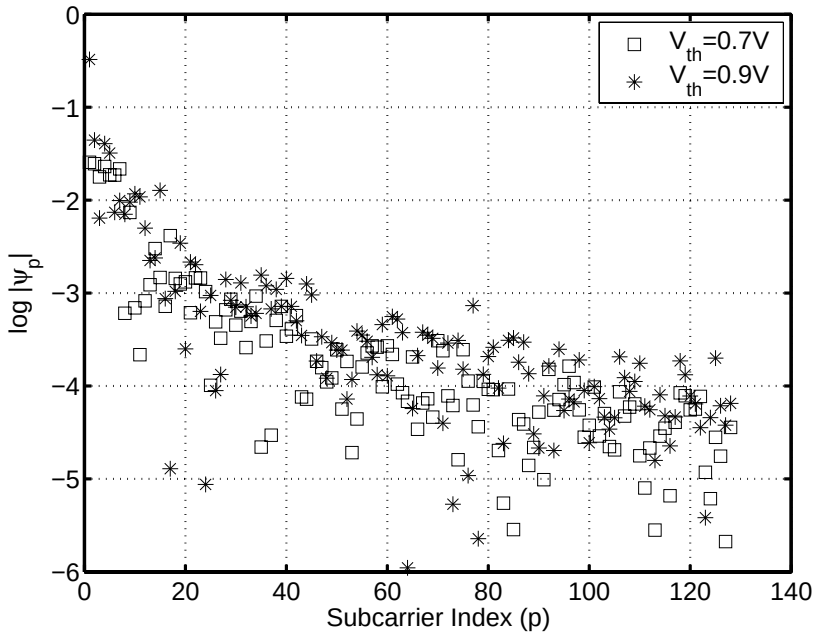

Figure 4.2. Sampled PSD of the phase noise for $V_{th} = 0.7$V and $V_{th} = 0.9$V.

the carrier p=0) possess a linear relationship with the subcarrier frequency index p approximately and they are very close to each other. Similar to the ICI mitigation for the general phase noise problem, we may utilize the aforementioned findings to improve the OFDM system performance when the hot carriers occur.

4.4 Simulation Results

Simulations were carried out for one hundred thousand random QPSK-OFDM, 16QAM-OFDM and 64QAM-OFDM symbols transmitted over an AWGN channel. Both SC-coded OFDM (denoted as "PCC" in the figures) and ordinary OFDM systems are considered. No pilot symbols were used for the CPE correction to test the worst scenario. It is also assumed that no carrier frequency offset exists. In all simulations, the number of subcarriers was set as N=128, while the threshold voltages were chosen as $V_{th} = 0.7$ volts and $V_{th} = 0.9$ volts.

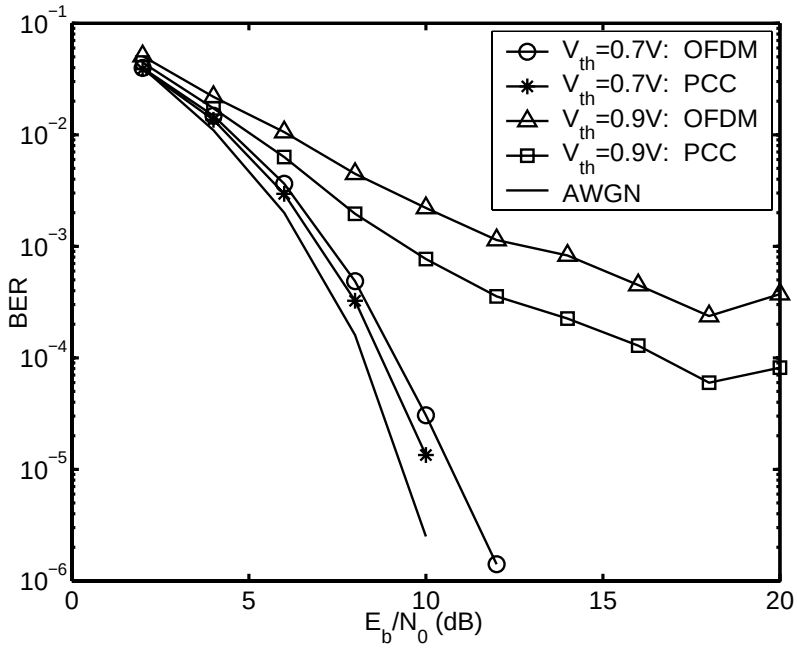

Figure 4.3. BER Performance for the ordinary and the SC-coded QPSK-OFDM systems, N=128.

According to Figures 4.3-4.5, the 64QAM-OFDM system is most and the QPSK-OFDM system is least sensitive to any subtle increase in the threshold voltage. The ICI dominates the phase noise for large N values [4]. The ICI and the AWGN affect the OFDM systems equivalently [4]. The higher threshold voltage, the higher phase noise power. Since the higher-order QAM modulation schemes are more sensitive to phase noises and ICI than the lower-order modulation schemes [41].

Figure 4.3 depicts the BER performances for an ordinary QPSK-OFDM system and an SC-coded QPSK-OFDM system. Note that the SC-coded OFDM system achieves an SNR (E_b/N_0) gain of 4 dB at BER = 2×10^{-4} with the threshold voltage 0.9 volts.

Figure 4.4 depicts the performances for ordinary and SC-coded 16QAM-OFDM systems. Here, the SC-coded OFDM system yields a 5-dB SNR gain at BER =10^{-3} for a threshold voltage of 0.7 volts.

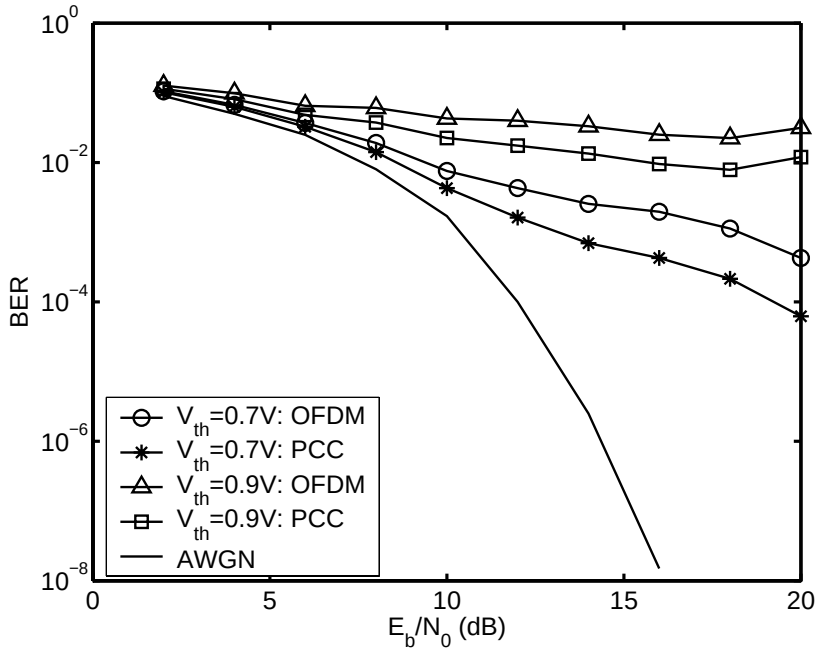

Figure 4.4. BER Performance for the ordinary and the SC-coded 16QAM-OFDM systems, *N*=128.

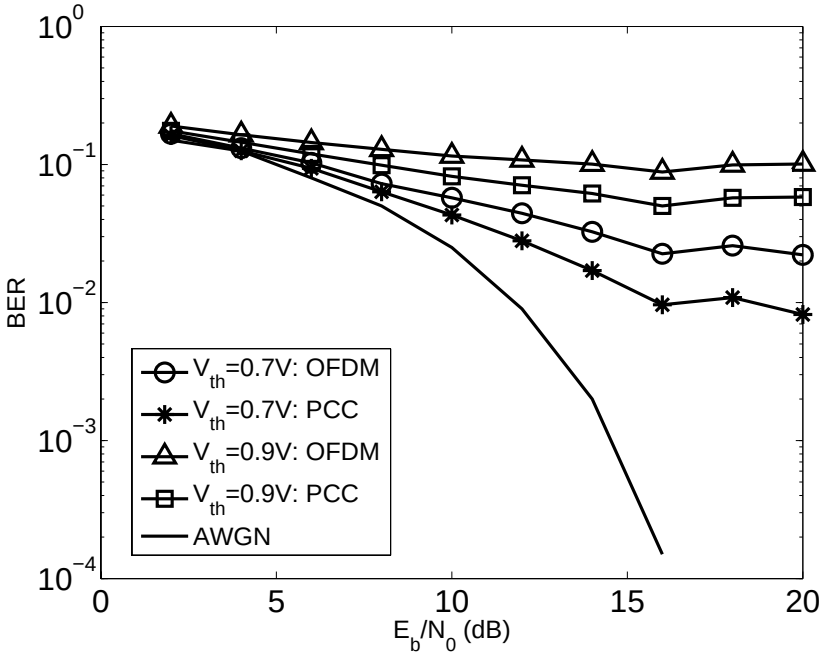

Figure 4.5 BER Performance for the ordinary and the SC-coded 64QAM-OFDM systems, *N*=128.

Figure 4.5 depicts the performances for ordinary and SC-coded 64QAM-OFDM systems. In this case, a 4-dB SNR gain is obtained at BER = 2×10^{-3} for the threshold voltage of 0.7 volts.

Our results illustrated in Figures 4.3-4.5 are very similar to those in [27] subject to the same phase noise variances. Therefore, the SC-coded OFDM scheme works quite well for combating the HC problem arising from the short-channel synchronization devices.

4.5 Chapter Summary

In Chapter 4, we investigate the performance of the ICI self-cancellation coding in the presence of the hot-carrier effect. Through our analysis and simulations, we have found that the ICI self-cancellation scheme is very promising for the OFDM performance enhancement.

A 4-dB SNR margin is achieved using the SC-coded QPSK-OFDM system at BER = 2×10^{-4} and V_{th} = 0.9V over the ordinary QPSK-OFDM, while the SC-coded 16QAM-OFDM system yields a 5-dB SNR gain at BER = 10^{-3} and V_{th} = 0.7V over the ordinary 16QAM-OFDM. Similarly, the SC-coded 64QAM-OFDM system yields a 4-dB SNR gain at BER = 2×10^{-2} and V_{th} = 0.7V, over the ordinary 64QAM-OFDM system.

Besides, the ICI self-cancellation coding is very simple to be inserted and implemented in any OFDM transceiver.

Chapter 5

Conclusions

In this dissertation, we have investigated the phase noise which arises from the hot carriers and studied the corresponding effect on the OFDM system performance. The HCs are the charge-carriers which have been highly energized by the electric fields inside the MOSFET devices. The HC effect is phenomenal in the *short-channel* MOSFET devices, and these short-channel MOSFETs are commonly seen in the modern wireless communication transceivers. We discuss the phase noise impact on both single-carrier wireless transceivers and multi-carrier (OFDM) wireless transceivers. We have also investigated the ICI self-cancellation coding as a means to combat the adverse effect of the phase noise arising from the HCs on the OFDM systems. The three underlying signal modulations were QPSK, 16-QAM and 64-QAM in our studies. In general, we have discovered that the wireless system performance can be related to a function of the threshold voltage variation caused by the HCs in the MOSFET-built VCO devices.

In depth, we have provided the exact analysis of the expected BER and the SINR performance degradation for the single-carrier QPSK systems, while the performances of the 16-QAM and 64-QAM systems were evaluated via computer simulations. Theoretically, we have proved that the asymptotical BER of the QPSK systems increases monotonically as the threshold voltage increases. Our analysis can serve for the design of the compact single-carrier wireless QAM transceivers which are built on the short-channel MOSFET devices.

Moreover, our asymptotic analysis provides the lower bound of the achievable BER for the systems which suffer from the phase noise due to the HC effect.

Through our analysis and simulation results, we also showed that an increased threshold voltage gives rise to the OFDM performance degradation. In particular, the 64-QAM-OFDM systems yield the most severely degraded performance due to the phase noise, while the QPSK-OFDM is least sensitive to the subtle threshold voltage increases. In addition, we derived the sensitivity function of the phase noise power spectral density (PSD), which helps explain the BER performance of the wireless OFDM system versus the threshold voltage. Furthermore, we showed that the BER performance evaluation using the existing phase noise models independent of the HCs can be different from that using our new phase noise model dependent on the HCs by up to three orders of magnitude.

It is noted that our system performance analysis utilizes the MOSFET threshold voltage as a crucial parameter. Since the MOSFET's threshold voltage can be easily measured or can be found in the device specifications, our BER and SINR analyses and simulation results provide the wireless system designers with the expected system BER or SINR performances. No such information can be drawn from any other existing phase noise model.

For combating the HC effect, we have investigated the ICI self-cancellation coding scheme and found that the simulation results are very promising. Although the performance of the SC-coded OFDM systems can be further improved by the employment of common phase error (CPE) correction schemes and the adaptive equalization, the additional hardware cost might be significant and it is beyond the scope of this dissertation work.

References

[1] F. M. Gardner, *Phaselock Techniques*, 2nd Edition, John Wiley and Sons, 1979.

[2] B. Sklar, *Digital Communications: Fundamentals and Applications*, 2nd Edition, Prentice-Hall, 2001.

[3] J. W. M. Bergmans, "Effect of loop delay on stability of discrete-time PLL," *IEEE Transactions on Circuits and Systems I: Fundamental Theory and Applications*, vol. 42, no. 4, pp. 229-231, April 1995.

[4] M. El-Tanany, Y. Wu and L. Hazy, "Analytical modeling and simulation of phase noise interference in OFDM-Based digital television terrestrial broadcasting systems," *IEEE Transactions on Broadcasting*, vol. 47, no. 1, pp. 20-31, March 2001.

[5] G. Liu and W. Zhu, "Compensation of phase noise in OFDM systems using an ICI reduction scheme," *IEEE Transactions on Broadcasting*, vol. 50, no. 4, pp. 399- 407, Dec. 2004.

[6] S. Naseh, M. J. Deen and O. Marinov, "Effects of hot-carrier stress on the performance of the LC-Tank CMOS oscillators," *IEEE Transactions on Electron Devices*, vol. 50, no. 5, pp. 1334-1339, May 2003.

[7] M. N. Horenstein, *Microelectronic Circuits and Devices*, 2nd Edition, Prentice Hall, 1996.

[8] ETSI EN 300 744 V1.4.1 (2001-01): "Digital video broadcasting (DVB); framing structure, channel coding and modulation for digital terrestrial television," ETSI, 2001.

[9] IEEE Standard 802.11a-1999, "Supplement to information technology—telecomm. and information exchange between systems—local and metropolitan-area networks—specific requirements—part 11: wireless LAN medium access control (MAC) and physical layer (PHY) specifications: high speed physical layer (PHY) in the 5 GHz band," 1999.

[10] IEEE Standard 802.11g-2003, "IEEE standard for information technology—telecommunications and information exchange between systems— local and metropolitan area networks — specific requirements part 11: wireless LAN medium access control (MAC) and physical layer (PHY) specifications amendment 4: further higher data rate extension in the 2.4 GHz band," 2003.

[11] IEEE Standard 802.16-2004, "Local and metropolitan area networks—Part 16: Air interface for fixed broadband wireless access systems," 2004.

[12] ETS 300 401 (1997): "Radio broadcasting systems; digital audio broadcasting (DAB) to mobile, portable and fixed receivers," ETSI, 1997.

[13] ETSI TS 101 999 V1.1.1 (2002-04): "Broadband radio access networks (BRAN), Hiperaccess: PHY protocol specification," ETSI, 2002.

[14] "Standard A/80: Modulation and coding requirements for digital TV (DTV) applications over satellite," Advanced Television Systems Committee, July 1999.

[15] "Recommended practice A/111: Design of synchronized multiple transmitter networks," Advanced Television Systems Committee, September 2004.

[16] E. Xiao, J. S. Yuan and H. Yang, "Hot-carrier and soft-breakdown effects on VCO performance," *IEEE Transactions on Microwave Theory and Techniques*, vol. 50, no. 11, pp. 2453-2458, November 2002.

[17] J-T. Park, B-J. Lee, D-W. Kim, C-G. Yu and H-K. Yu, "RF performance degradation in nMOS transistors due to hot-carrier stress," *IEEE Transactions on Electron Devices*, vol. 47, no. 5, pp. 1068-1072, May 2000.

[18] H.-C. Wu and X. Huang, "Joint phase/amplitude estimation and symbol detection for wireless ICI self-cancellation coded OFDM systems," *IEEE Transactions on Broadcasting*, vol. 50, no. 1, pp. 49-55, March 2004.

[19] H.-C. Wu and G. Gu, "Analysis of intercarrier and interblock interferences in wireless OFDM systems," *Proceedings of the IEEE Global Telecommunications Conferenc*e, vol. 2, pp.784-788, December 2003.

[20] A. Hazmi, J. Rinne and M. Renfors, "DVB-T signal over cable TV network and phase noise requirements," *Proceedings of the IEEE Workshop on Signal Processing Advances in Wireless Communications*, pp. 166-169, March 2001.

[21] A.G. Armada and M. Calvo, "Phase noise and subcarrier spacing effects on the performance of an OFDM communication system," *IEEE Communications Letters*, vol. 2, no. 1, pp. 11-13, January 1998.

[22] A.G. Armada, "Understanding the effects of phase noise in orthogonal frequency division multiplexing (OFDM)," *IEEE Transactions on Broadcasting*, vol. 47, no. 2, pp. 153-159, June 2001.

[23] C. Muschallik, "Influence of RF oscillators on an OFDM signal," *IEEE Transactions on Consumer Electronics*, vol. 41, no. 3, pp. 592-603, August 1995.

[24] S. Wu and Y. Bar-Ness, "OFDM systems in the presence of phase noise: consequences and solutions," *IEEE Transactions on Communications*, vol. 52, no. 11, pp. 1988-1996, November 2004.

[25] P. Robertson and S. Kaiser, "Analysis of the effects of phase noise in orthogonal frequency division multiplex (OFDM) systems," *Proceedings of the IEEE International Conference on Communications*, pp. 1652-1657, June 1995.

[26] J. Stott, "The effects of phase noise in COFDM," *EBU Technical Review*, No. 276, 1998.

[27] J. Shentu, K. Panta and J. Armstrong, "Effects of phase noise on performance of OFDM systems using an ICI cancellation scheme," *IEEE Transactions on Broadcasting*, vol. 49, no. 2, pp. 221-224, June 2003.

[28] J. Zhang, H. Rohling and P. Zhang, "Analysis of ICI cancellation scheme in OFDM systems with phase noise," *IEEE Transactions on Broadcasting*, vol. 50, no. 2, pp. 97-106, Jun. 2004.

[29] B. Stantchev and G. Fettweis, "Time-variant distortions in OFDM," *IEEE Communications Letters*, vol. 4, no. 9, pp. 312-314, September 2000.

[30] R. Hasholzner, C. Drewes and J. S. Hammerschmidt, "The effects of multiple access schemes on equalization for broadband wireless local loop systems," *Proceedings of the IEEE Vehicular Technology Conference*, vol. 2, pp. 1305-1309, 1998.

[31] T. Pollet, M. Van Bladel and M. Moeneclaey, "BER sensitivity of OFDM systems to carrier frequency offset and wiener phase noise," *IEEE Transactions on Communications*, vol. 43, no. 2/3/4, pp. 191-193, February/March/April 1995.

[32] T. Pollet, M. Moeneclaey, I. Jeanclaude and H. Sari, "Effect of carrier phase jitter on single-carrier and multi-carrier QAM systems," *Proceedings of the IEEE International Conference on Communications*, vol. 2, pp. 1046-1050, 1995.

[33] A. Georgiadis, "Gain, phase imbalance, and phase noise effects on error vector magnitude," *IEEE Transactions on Vehicular Technology*, vol. 53, no. 2, pp. 443-449, March 2004.

[34] Z. Jianhua, H. Rohling and Z. Ping, "Analysis of ICI cancellation scheme in OFDM systems with phase noise," *IEEE Transactions on Broadcasting*, vol. 50, no. 2, pp. 97-106, June 2004.

[35] S. Wu. And Y. Bar-Ness, "A phase noise suppression algorithm for OFDM-based WLANs," *IEEE Communications Letters*, vol. 6, no. 12, pp. 535-537, December 2002.

[36] M.R.Gholami, A. Nader-Esfahani and A.A. Eftekhar, “A new method of phase noise compensation in OFDM,” *IEEE International Conference on Communications*, vol. 5, pp. 3443-3446, May 2003.

[37] S. Herlekar, H.-C. Wu, C. Zhang and A. Srivastava, “OFDM performance analysis in the presence of synchronization errors induced by hot carriers,” *Proceedings of the 62nd IEEE Vehicular Technology Conference (VTC)*, vol. 3, pp. 1844-1848, September 2005.

[38] C. Zhang, and A. Srivastava, "Hot-carrier effects on jitter and phase noise in CMOS voltage-controlled oscillators," *Proceedings of the SPIE International Symposium on Fluctuations and Noise*, vol. 5844, pp. 52-62, May 2005.

[39] C. Zhang, A. Srivastava and H.C. Wu, "Hot-electron-induced effects on noise and jitter in submicron CMOS phase-locked loop circuits," *Proceedings of the 48th IEEE Midwest Symposium on Circuits and Systems*, 2005, in press.

[40] A.-S. Porret, T. Melly, D. Python, C. C. Enz and E. A. Vittoz, “An ultralow-power UHF transceiver integrated in a standard digital CMOS process: architecture and receiver,” *IEEE Journal of Solid-State Circuits*, vol. 36, no. 3, pp. 452-466, March 2001.

[41] J. G. Proakis, *Digital Communications*, 4th Edition, McGraw-Hill, 2001.

[42] A. Demir, “Phase noise and timing jitter in oscillators with colored noise sources,” *IEEE Transactions on Circuits and Systems I: Fundamental Theory and Applications*, vol. 49, no. 12, pp. 1782-1791, December 2002.

[43] A. Hajimiri, S. Limotyrakis and T.H. Lee, “Jitter and phase noise in ring oscillators,” *IEEE Journal of Solid State Circuits*, vol. 34, no. 6, pp. 790-804, June 1999.

[44] A. Fakhr, M. J. Deen and H. DeBruin, “Low-voltage, low-power and low phase noise 2.4 GHz VCO for medical wireless telemetry,” *Proceedings of the Canadian Conference on Electrical and Computer Engineering*, vol. 3, pp. 1321-1324, 2004.

[45] S. Herlekar, C. Zhang, H-C. Wu and A. Srivastava, “Phase noise analysis for OFDM systems based on Hot-carrier effects in synchronization electronics,” *Proceedings of the SPIE International Symposium on Fluctuations and Noise*, vol. 5847, pp. 150-159, 2005.

[46] X. Tang, M-S. Alouini and A. J. Goldsmith, “Effect of channel estimation error on M-QAM BER performance in rayleigh fading,” *IEEE Transactions on Communications,* vol. 47, no. 12, pp. 1856-1864, December 1999.

[47] L. Hanzo, M. Munster, B. J. Choi and T. Keller, *OFDM and MC-CDMA for Broadband Multi-User Communications, WLANs and Broadcasting*. John Wiley & Sons, West Sussex, England, 2003.

[48] P. Z. Peebles, Jr., Probability, Random Variables and Random Signal Principles, 4th Edition, McGraw-Hill, 2001.

[49] H. L. Royden, *Real Analysis*, 3rd Edition, Prentice-Hall, New Jersey, 1988.

[50] A. Papoulis and U. Pillai, *Probability, Random Variables and Stochastic Processes*, 4th Edition, McGraw-Hill, 2002.

[51] J. A. C. Bingham, "Multi-carrier modulation for data transmission: an idea whose time has come," *IEEE Communications Magazine*, vol. 28, no. 5, pp. 5-14, May 1990.

[52] ITU Recommendations G.992.1, "Asymmetric digital subscriber line (DSL) transceivers," ITU, June 1999.

[53] J.S. Chow, J. C. Tu and J. M. Cioffi, "A discrete multitone transceiver system for HDSL applications," *IEEE Journal on Selected Areas in Communications*, vol. 9, no. 6, pp. 895-908, August 1991.

[54] G. Ginis and J. M. Cioffi, "Vectored transmission for digital subscriber line systems," *IEEE Journal on Selected Areas in Communications*, vol. 20, no. 5, pp. 1085-1104, June 2002.

[55] C. Zeng and J. M. Cioffi, "Near-end crosstalk mitigation in ADSL systems," *IEEE Journal on Selected Areas in Communications*, vol. 20, no. 5, pp. 949-958, June 2002.

[56] S. Weinstein and P. Ebert, "Data transmission by frequency-division multiplexing using the discrete fourier transform," *IEEE Transactions on Communications*, vol. 19, no. 5, part 1, pp. 628 - 634, October 1971.

[57] L. Cimini Jr., "Analysis and simulation of a digital mobile channel using orthogonal frequency division multiplexing," *IEEE Transactions on Communications*, vol. 33, no. 7, pp. 665-675, July 1985.

[58] M. Speth, S. A. Fechtel, G. Fock and H. Meyr, "Optimum receiver design for wireless broad-band systems using OFDM - Part I," *IEEE Transactions on Communications*, vol. 47, no. 11, pp. 1668-1677, November 1999.

[59] H. Sari, G. Karam and I. Jeanclaude, "Transmission techniques for digital terrestrial TV broadcasting," *IEEE Communications Magazine*, vol. 33, no. 2, pp. 100–109, February 1995.

[60] T. S. Rappaport, *Wireless Communications Principles and Practice*, Prentice-Hall, 1996.

[61] J. Armstrong, "Analysis of new and existing methods of reducing intercarrier interference due to carrier frequency offset in OFDM," *IEEE Transactions on Communications*, vol. 47, no. 3, pp. 365-369, March 1999.

[62] Y. Zhao and S.-G. Haggman, "Intercarrier interference selfcancellation scheme for OFDM mobile communication systems," *IEEE Transactions on Communications*, vol. 49, no. 7, pp. 1185-1191, July 2001.

[63] C.-T. Chen, *Signals and Systems*, 3rd Edition, Oxford University Press, 2004.

[64] S. Kaiser (private communication), 2005.

Appendix A: Calculation of Error Probability

In this section, we will derive the theoretical probability that the MSB of the received symbol $r(n)$ is detected incorrectly, given that the signal $\bar{s}_1$ from the QPSK signal constellation in Figure 2.2 was transmitted. According to Figure 2.3, it is noted that the transmitted MSB with the actual value *zero* is detected incorrectly if $r_R(n) < 0$, where $r_R(n)$ is given by Eq. (2.4). Therefore, we can write

$$\begin{aligned} P\left[\varepsilon_{MSB} \mid \bar{s}_1\right] &= P\left[w_R(n) < -\sqrt{E_s/2}\left(\cos\theta_n - \sin\theta_n\right)\right] \\ &= P\left[w_R(n) > \sqrt{E_s/2}\left(\cos\theta_n - \sin\theta_n\right)\right] \\ &= \int_{-\infty}^{+\infty} P\left[w_R(n) > \sqrt{\frac{E_s}{2}}\left(\cos\theta_n - \sin\theta_n\right) \middle| \theta_n \right] p_\Theta(\theta_n)\, d\theta_n \end{aligned} \quad , \qquad \text{(A.1)}$$

where

$$P\left[w_R(n) > \sqrt{\frac{E_s}{2}}\left(\cos\theta_n - \sin\theta_n\right) \middle| \theta_n \right] = \int_{\nabla}^{+\infty} \frac{1}{\sqrt{2\pi\sigma_w^2}} \exp\left[\frac{-w_1^2}{2\sigma_w^2}\right] dw_1, \qquad \text{(A.2)}$$

$$\nabla \overset{\Delta}{=} \sqrt{\frac{E_s}{2}}\left(\cos\theta_n - \sin\theta_n\right), \qquad \text{(A.3)}$$

and the probability density function $p_\Theta(\theta_n)$ of the zero-mean Gaussian phase noise process is given by

$$p_\Theta(\theta_n) = \frac{1}{\sqrt{2\pi\lambda^2}} \exp\left[\frac{-\theta_n{}^2}{2\lambda^2}\right], \qquad -\infty < \theta_n < \infty. \qquad \text{(A.4)}$$

According to Eqs. (A.1)-(A.4), we can formulate $P\left[\varepsilon_{MSB} \mid \bar{s}_1\right]$ as

$$P[\varepsilon_{MSB} \mid \bar{s}_1] = \frac{1}{\sqrt{2\pi\lambda^2}} \int_{-\infty}^{+\infty} Q\left[\sqrt{\frac{E_s}{2\sigma_w^2}}\left(\cos\theta_n - \sin\theta_n\right)\right] \exp\left[\frac{-\theta_n{}^2}{2\lambda^2}\right] d\theta_n, \qquad \text{(A.5)}$$

where $Q(\cdot)$ is the *Gaussian tail probability* [41].

Appendix B: Proof of Error Probability as a Monotonic Increasing Function of Threshold Voltage

In this section, we will prove that

$$\frac{dJ_{il}(\lambda)}{d\lambda} > 0,\ 1 \geq \lambda \geq 0,\ i = 1,2,3, \text{ and } l = \mathsf{Z}^{+} \cup \{0\}, \tag{B.1}$$

where

$$J_{il}(\lambda) \overset{\Delta}{=} Q\left(\frac{a_{il}}{\lambda}\right) - Q\left(\frac{b_{il}}{\lambda}\right),\ b_{il} > a_{il} > 0. \tag{B.2}$$

Lemma: Given a function $J_{il}(\lambda) \overset{\Delta}{=} Q\left(\frac{a_{il}}{\lambda}\right) - Q\left(\frac{b_{il}}{\lambda}\right)$ where $b_{il} > a_{il} > 0$, then $J_{il}(\lambda)$ is monotonically increasing with respect to λ, for $0 < \lambda^2 < B_{il}(a_{il}, b_{il})$, where $B_{il}(a_{il}, b_{il}) = \frac{b_{il}^2 - a_{il}^2}{2\left[\ln(b_{il}) - \ln(a_{il})\right]}$.

Proof:

If $0 < \lambda^2 < \frac{b_{il}^2 - a_{il}^2}{2\left[\ln(b_{il}) - \ln(a_{il})\right]}$, then

$$\ln\left(\frac{a_{il}}{b_{il}}\right) + \frac{b_{il}^2 - a_{il}^2}{2\lambda^2} > 0. \tag{B.3}$$

By taking the exponential function on both sides of Eq. (B.3), we obtain

$$a_{il}\, e^{-\frac{a_{il}^2}{2\lambda^2}} - b_{il}\, e^{-\frac{b_{il}^2}{2\lambda^2}} > 0. \tag{B.4}$$

Let $J_{il}(\lambda) \overset{\Delta}{=} Q\left(\frac{a_{il}}{\lambda}\right) - Q\left(\frac{b_{il}}{\lambda}\right)$, where $b_{il} > a_{il} > 0$. We can then derive

$$\frac{dJ_{il}(\lambda)}{d\lambda} = \frac{a_{il}}{\lambda^2}\frac{1}{\sqrt{2\pi}}\, e^{-\frac{a_{il}^2}{2\lambda^2}} - \frac{b_{il}}{\lambda^2}\frac{1}{\sqrt{2\pi}}\, e^{-\frac{b_{il}^2}{2\lambda^2}}, \tag{B.5}$$

where Leibnitz's rule has been used to calculate the derivative in Eq. (B.5) [50]. According to Eqs. (B.4) and (B.5),

$$\frac{dJ_{il}(\lambda)}{d\lambda} > 0,\ 0 < \lambda^2 < B_{il}(a_{il}, b_{il}). \tag{B.6}$$

According to Eq. (2.26),

$$a_{1l} = \beta_{1l} = \pi/4 + 2l\pi,\ a_{2l} = b_{1l} = \beta_{2l} = 3\pi/4 + 2l\pi,$$

$$a_{3l} = b_{2l} = \beta_{3l} = 5\pi/4 + 2l\pi,\ b_{3l} = \beta_{4l} = 7\pi/4 + 2l\pi.$$

It can be shown that $B_{il}(a_{il}, b_{il}) > 1$, $i = 1,2,3$, and $l = \mathsf{Z}^+$. Thus $\frac{dJ_{il}(\lambda)}{d\lambda} > 0$, $1 \geq \lambda \geq 0$, $i = 1,2,3$, and $l = \mathsf{Z}^+ \cup \{0\}$.

Vita

Sameer R. Herlekar was born in Bangalore, India, on November 4, 1976. He received the degree Bachelor of Engineering (Hons.) in Electronics and Instrumentation, and the degree Master of Science (Hons.) in Mathematics, both from Birla Institute of Technology and Science, Pilani, India, in 1999. He entered the graduate program in the Department of Electrical and Computer Engineering at Louisiana State University (LSU) in 1999. He received the degree Master of Science in Electrical Engineering from LSU in 2001. He is now a candidate for the degree of Doctor of Philosophy in electrical engineering.